Article

Cell Chemical Biology

Identification of the Nicotinamide Salvage Pathway as a New Toxification Route for Antimetabolites

Graphical Abstract

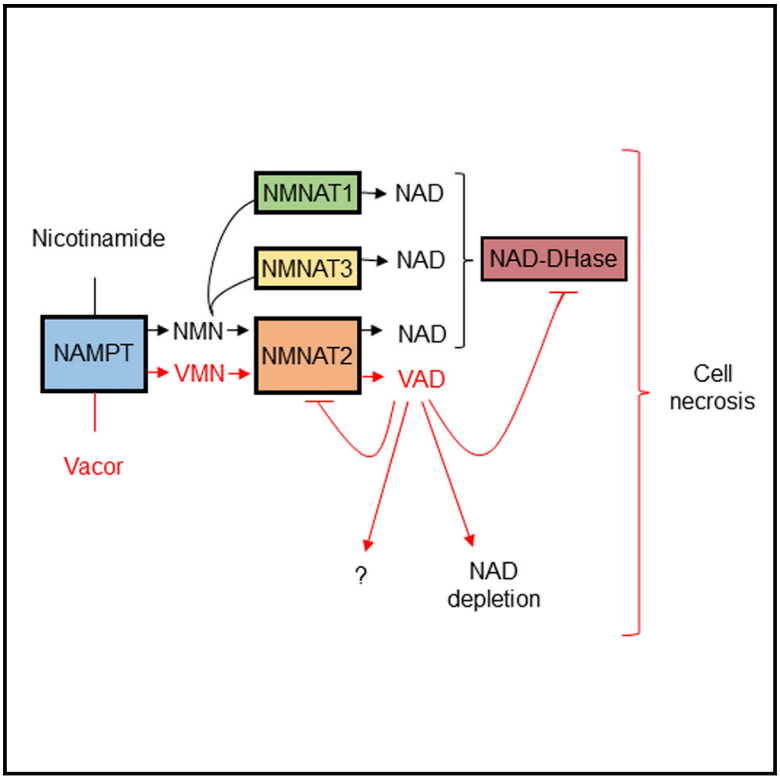

Authors

Daniela Buonvicino, Francesca Mazzola, Federica Zamporlini, ..., Barbara Stecca, Nadia Raffaelli, Alberto Chiarugi

Correspondence

alberto.chiarugi@unifi.it

In Brief

Synthesis and consumption of the pyridine nucleotide NAD are increased in cancer cells and contribute to cell proliferation and neoplastic transformation. Buonvicino et al. identified Vacor as a new structure interfering with NAD metabolome which may lead to the development of new antineoplastic molecules.

Highlights

- NAMPT and NMNAT2 metabolize Vacor into the NAD analog VAD
- Vacor metabolism prompts NAD depletion and NAD-dependent dehydrogenase inhibition
- Vacor triggers necrosis of cancer cells and tumor xenografts expressing NMNAT2
- The nicotinamide salvage pathway can be harnessed for antimetabolic strategies

Buonvicino et al., 2018, Cell Chemical Biology *25*, 471–482
April 19, 2018
https://doi.org/10.1016/j.chembiol.2018.01.012

CellPress

Cell Chemical Biology
Article

Identification of the Nicotinamide Salvage Pathway as a New Toxification Route for Antimetabolites

Daniela Buonvicino,[1] Francesca Mazzola,[2] Federica Zamporlini,[3] Francesco Resta,[4] Giuseppe Ranieri,[1] Emidio Camaioni,[5] Mirko Muzzi,[1] Riccardo Zecchi,[6] Giuseppe Pieraccini,[6] Christian Dölle,[7] Massimo Calamante,[8] Gianluca Bartolucci,[4] Mathias Ziegler,[7] Barbara Stecca,[9] Nadia Raffaelli,[3] and Alberto Chiarugi[1,10,*]

[1]Department of Health Sciences, Section of Clinical Pharmacology and Oncology, University of Florence, Florence 50139, Italy
[2]Department of Clinical Science, Polytechnic University of Marche, Ancona 60131, Italy
[3]Department of Agricultural, Food and Environmental Sciences, Polytechnic University of Marche, Ancona 60131, Italy
[4]Department of Neurosciences, Psychology, Drug Research and Child Health, University of Florence, Florence 50139, Italy
[5]Department of Pharmaceutical Sciences, University of Perugia, Perugia 06123, Italy
[6]Mass Spectrometry Service Centre (CISM), University of Florence, Florence 50139, Italy
[7]Department of Molecular Biology, University of Bergen, 5020 Bergen, Norway
[8]Department of Chemistry, University of Florence, Florence 50019, Italy
[9]Core Research Laboratory-Istituto Toscano Tumori, Department of Oncology, Careggi University Hospital, Florence 50139, Italy
[10]Lead Contact
*Correspondence: alberto.chiarugi@unifi.it
https://doi.org/10.1016/j.chembiol.2018.01.012

SUMMARY

Interest in the modulation of nicotinamide adenine dinucleotide (NAD) metabolome is gaining great momentum because of its therapeutic potential in different human disorders. Suppression of nicotinamide salvage by nicotinamide phosphoribosyl transferase (NAMPT) inhibitors, however, gave inconclusive results in neoplastic patients because several metabolic routes circumvent the enzymatic block converging directly on nicotinamide mononucleotide adenylyl transferases (NMNATs) for NAD synthesis. Unfortunately, NMNAT inhibitors have not been identified. Here, we report the identification of Vacor as a substrate metabolized by the consecutive action of NAMPT and NMNAT2 into the NAD analog Vacor adenine dinucleotide (VAD). This leads to inhibition of both enzymes, as well as NAD-dependent dehydrogenases, thereby causing unprecedented rapid NAD depletion, glycolytic block, energy failure, and necrotic death of NMNAT2-proficient cancer cells. Conversely, lack of NMNAT2 expression confers complete resistance to Vacor. Remarkably, Vacor prompts VAD formation and growth suppression in NMNAT2-positive neuroblastoma and melanoma xenografts. Our data show the first evidence of harnessing the entire nicotinamide salvage pathway for antimetabolic strategies.

INTRODUCTION

Targeting of metabolic pathways selectively activated in cancer cells appears promising as a single or add-on antineoplastic therapy (Boroughs and Deberardinis, 2015; Deberardinis and Chandel, 2016). In particular, suppression of metabolic rescue of nicotinamide (the so-called NAD rescue pathway) in tumors has been exploited at the preclinical and clinical levels (Chiarugi et al., 2012). The rationale behind this metabolic strategy is related to the key role of nicotinamide adenine dinucleotide (NAD) in energetic metabolism (Canto et al., 2015), and also to the notion that NAD consumption is increased in cancer cells, two features that sensitize the neoplasm to drugs reducing NAD neoformation. Consistently, impairment of NAD resynthesis by selective inhibition of the rate-limiting enzyme nicotinamide phosphoribosyl transferase (NAMPT) showed efficacy in preclinical tumor models, and also reached the clinical arena with only partially positive results (Sampath et al., 2015; Shackelford et al., 2013). In principle, however, blockade of NAD resynthesis by NAMPT inhibition can be circumvented by additional metabolic pathways leading to NAD formation such as those operated by nicotinic acid phosphoribosyl transferase or quinolinic acid phosphoribosyl transferase (Bogan and Brenner, 2008). These enzymes convert nicotinic acid or quinolinic acid into nicotinic acid mononucleotide, which is then converted into NAD, thereby bypassing NAMPT block (Piacente et al., 2017). Even the nicotinamide riboside (NR) kinase-dependent pathway (Bieganowski and Brenner, 2004) transforming NR into NAD via nicotinamide mononucleotide (NMN) can bypass NAMPT inhibition (Sociali et al., 2016). Inevitably, these alternative pathways provide extra NAD to cells, thereby reducing the metabolic impact and lethality of NAMPT inhibitors. It is worth noting that although NAMPT is the rate-limiting step of the nicotinamide salvage pathway, nicotinamide mononucleotide adenylyl transferase (NMNAT) is the sole enzyme operating the last step of NAD (re)synthesis on which all the aforementioned metabolic routes converge to refill NAD stores (Berger et al., 2005). NMNAT inhibition, therefore, might dramatically compromise NAD biosynthesis, and potentiate the metabolic consequences of a concomitant pharmacological suppression of NAMPT activity. Unfortunately, potent, selective, and cell-permeable

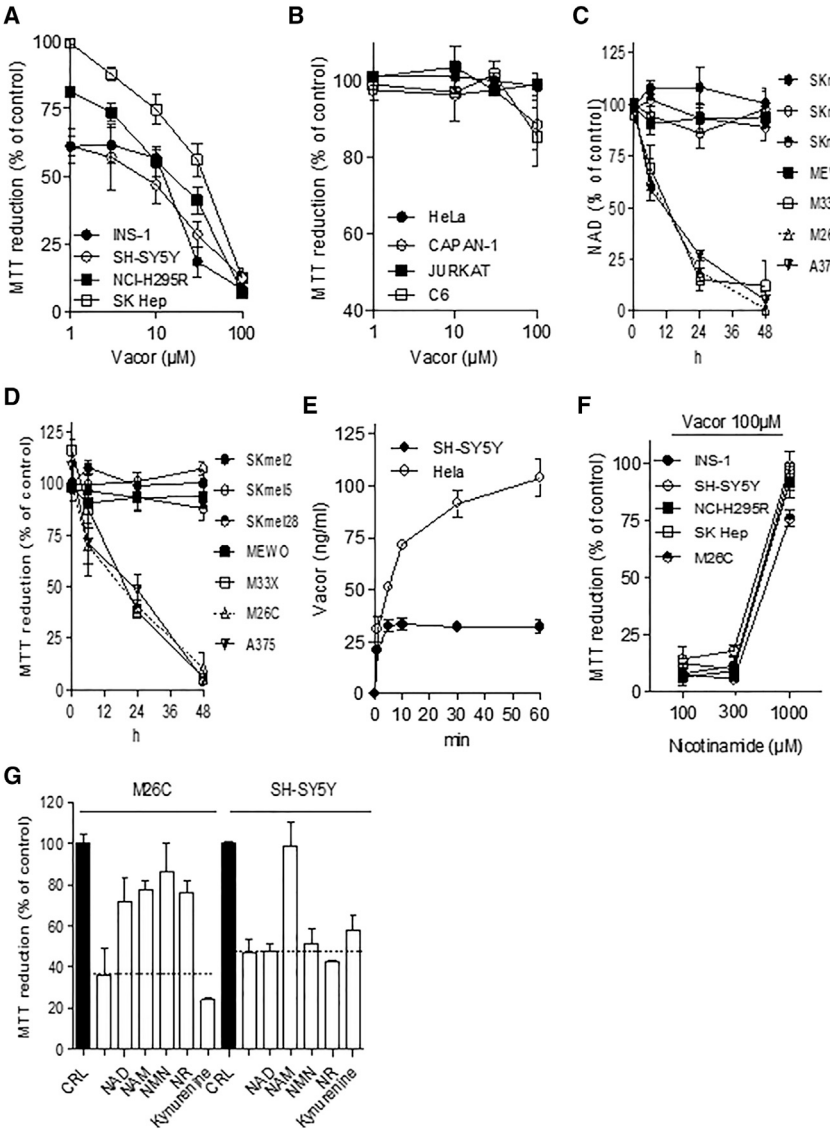

Figure 1. Effect of Vacor on NAD Content and Survival of Different Cell Lines

(A–D) Dose effect of Vacor on sensitive (A) and insensitive (B) cell lines at 24-hr incubation. Effect of 100 μM Vacor on different melanoma cell lines over time on NAD content (C) and viability (D).

(E) Time-dependent intracellular Vacor accumulation (used at 100 μM) in SH-SY5Y and HeLa cells.

(F) Effects of nicotinamide on Vacor (100 μM/24 hr) cytotoxicity.

(G) Effect of different NAD precursors (1 mM) on Vacor cytotoxicity (100 μM/12 hr). Each point/bar represents the mean ± SEM of at least 3 experiments.

NMNAT inhibitors still wait to be identified. Thus, it is unknown how intracellular NAD metabolism and cellular homeostasis are affected in conditions of complete inhibition of the nicotinamide salvage pathway. Such information would be relevant for a deeper understanding of the NAD metabolome, for the design of more potent tumor cell killing strategies based on metabolic approaches, and for the identification of rescue therapies designed to spare healthy tissues from the effects of NAD-depleting agents.

In this study, we screened a new series of compounds bearing a new pharmacophore of NAMPT inhibitors, and identified a lead, previously known as Vacor (pyrinuron; Lewitt, 1980), as a compound able to be originally converted by the consecutive action of NAMPT and NMNAT into the NAD antimetabolite Vacor adenine dinucleotide (VAD). We show that Vacor prompts extremely rapid derangement of NAD homeostasis, energetic metabolism, and cytotoxic activity only in NMNAT2-proficient tumor cell lines and xenografts.

RESULTS

Vacor Selectively Impairs NAD Metabolism and Cell Viability

Prior work indicates that NAMPT can metabolize specific inhibitors into phosphoribosyl derivatives. In particular, chemicals bearing the 3-pyridinyl ring bound to a urea or amide group behave as substrates and undergo an enzyme-catalyzed condensation with phosphoribosyl pyrophosphate (PRPP) into the NAMPT active site (Oh et al., 2014; Sampath et al., 2015). Thus, to identify substituted pyridine derivatives able to interfere with the NAD metabolome, we screened a series of compounds bearing the pyridinylmethyl-urea moiety, a structure similar to the pharmacophore of the prototypical NAMPT inhibitors FK866 and GMX1778 (Figure S1A) (Galli et al., 2013). Depletion of NAD content and death of SH-SY5Y neuroblastoma cells were adopted as screening parameters for the single compounds. Remarkably, notwithstanding the structural similarity of the chemicals, only compound **6** (3-(4-nitrophenyl)-1-(pyridin-3-ylmethyl)urea) depleted NAD pools and caused cell death (Figures S1B and S1C). Unexpectedly, we found that compound **6** is the old rodenticide Vacor (also known as Purynor). Curiously enough, Vacor intoxication in humans can be efficiently treated by intravenous injection of the metabolic NAD precursor nicotinamide (Lewitt, 1980). Surprisingly, a careful analysis of the literature revealed that the pharmacodynamic mechanisms underlying this antidotal effect have never been investigated. Being intrigued by this finding, we then screened Vacor against different cell types, and found that in addition to neuroblastoma, Vacor caused rapid death of INS-1 (insulinoma), NCI-H295R (adrenal corticocarcinoma) and SK-HEP (hepatocarcinoma) cells, whereas Capan-1 (pancreas adenocarcinoma), C6 (glioma), HeLa (cervix adenocarcinoma), and Jurkat (T cell leukemia) cells were completely insensitive to Vacor (Figures 1A and 1B). We also tested Vacor on different human melanoma cell lines because of the overexpression of NAMPT in this neoplasm

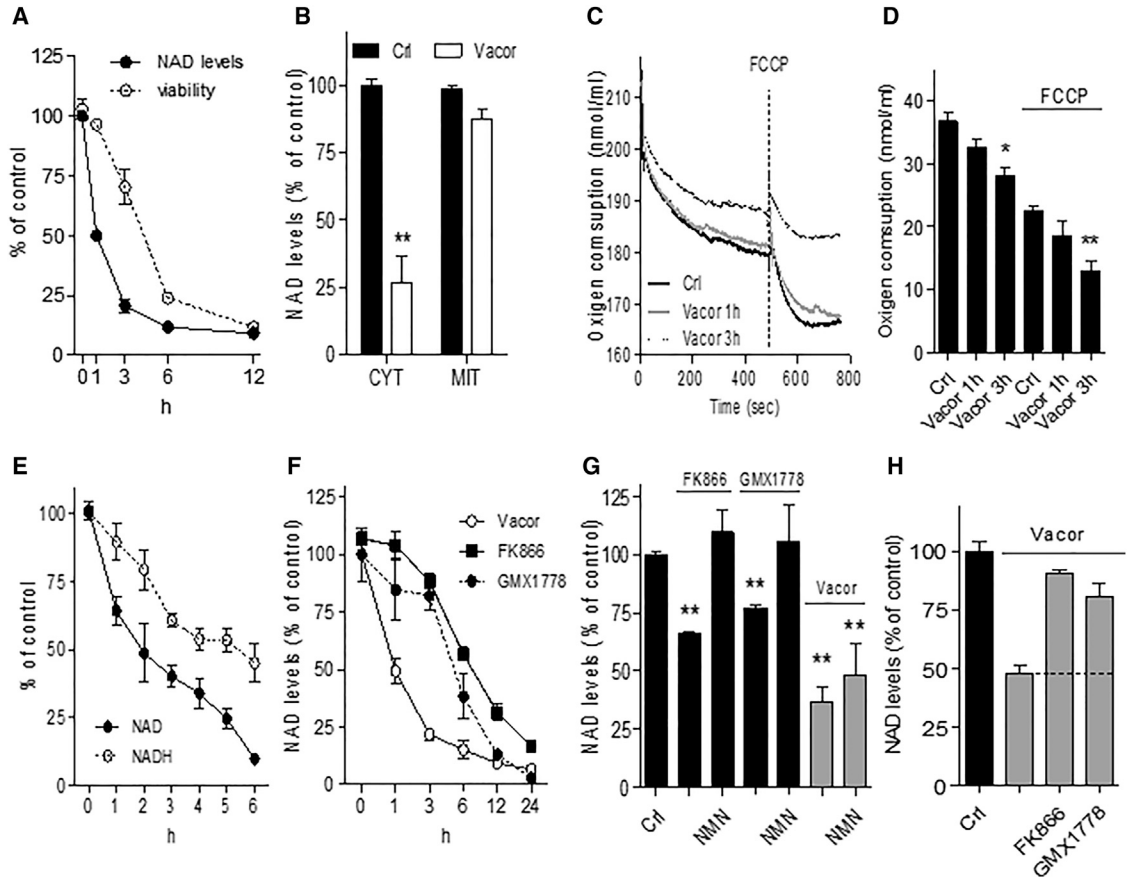

Figure 2. Effects of Vacor on Different Biochemical and Functional Parameters of Neuroblastoma SH-SY5Y Cells

(A) Comparison of the temporal kinetics of NAD depletion and cell death (propidium iodide staining) induced by Vacor (100 μM) in SH-SY5Y cells.

(B) Cytosolic and mitochondrial NAD content in SH-SY5Y exposed to Vacor (100 μM/1 hr).

(C and D) Representative (C) or quantitative (D) analysis of oxygen consumption by neuroblastoma cells exposed for 1 hr or 3 hr to Vacor (100 μM). The protonophore FCCP (carbonyl cyanide p-trifluoromethoxyphenylhydrazone) was used at 1 μM.

(E and F) Temporal kinetics of NADH depletion in comparison with that of NAD in neuroblastoma cells exposed to Vacor (100 μM). Comparison of the temporal kinetics of NAD depletion (F) in neuroblastoma SH-SY5Y cells exposed to Vacor, FK866, or GMX1778 (all at 100 μM).

(G) Rescue effect of NMN (1 mM) added to the growth medium of neuroblastoma SH-SY5Y cells exposed to Vacor, FK866, or GMX1778 (all at 100 μM/6 hr).

(H) Effects of FK866 or GMX1778 (all at 100 μM) on NAD contents of SH-SY5Y cells exposed to Vacor (100 μM/1 hr). Each point/bar represents the mean ± SEM of at least 3 experiments.

*$p < 0.05$, **$p < 0.01$ versus control (Crl) by ANOVA and Tukey's post hoc test.

(Maldi et al., 2013). We found that only three of them underwent NAD loss and cell death when exposed to the compound (Figures 1C and 1D). We next compared how intracellular Vacor contents rise over time in sensitive and insensitive cells, and unexpectedly found that they increased more in HeLa (insensitive) than in SH-SY5Y (sensitive) cells (Figure 1E), thus ruling out that selective toxicity was due to pharmacokinetic issues. Notably, in keeping with clinical evidence, nicotinamide dose-dependently prevented Vacor cytotoxicity (Figure 1F). However, other metabolic NAD intermediates (with the exception of kynurenine) and NAD itself protected melanoma but not neuroblastoma cells (Figure 1G). The latter, however, were protected when nicotinamide mononucleotide (NMN) was used at 10 mM (not shown). It is well known that poly(ADP-ribose) polymerase (PARP)-1 hyperactivation completely exhaust the intracellular NAD pool (Chiarugi, 2002). Hence, to understand whether PARP-1 activation concurs with NAD loss by Vacor, we tested the effects of three different PARP-1 inhibitors, and found that they did not affect dinucleotide depletion (Figure S1D).

Effects of Vacor on Cellular NAD Homeostasis

We next attempted to characterize the temporal relationship between NAD depletion and death in SH-SY5Y cells exposed to Vacor. Notably, NAD depletion preceded cell death by some hours when evaluated by means of propidium iodide staining (Figure 2A). Cell fractionation experiments showed that 1 hr after Vacor exposure, NAD shortage already occurred in the cytosol but not in mitochondria (Figure 2B). In keeping with this, we found that mitochondrial membrane potential was unaltered in SH-SY5Y cells 1 hr after the Vacor challenge (Figures S2A and S2B), a time point corresponding to an almost 50% depletion of the whole cellular dinucleotide content. Likewise, oxygen consumption was unaffected in cells exposed for 1 hr to Vacor, being evident, however, 3 hr after the challenge (Figures 2C

and 2D). Also consistent with sparing of mitochondria homeostasis at early time points after Vacor exposure, depletion of NADH, which is more concentrated in the organelles than in cytosol, was delayed compared with that of NAD (Figure 2E).

Even though the structural analogy of Vacor with prototypical NAMPT inhibitors FK866 and GMX1778 (Figure S1A) suggested an involvement of NAMPT in the metabolic effects of Vacor, kinetics of both NAD drop and cell death were much more rapid in cells exposed to Vacor than in those challenged with FK866 or GMX1778 (Figures 2F and S2C). This important finding suggested that NAMPT inhibition cannot exclusively explain Vacor's effects. In keeping with this, NMN, the enzymatic product of NAMPT, fully prevented NAD drop by FK866 or GMX1778 but not that prompted by Vacor (Figure 2G). Collectively, different hints indicated that the impact of Vacor on NAD metabolome was different from that prompted by NAMPT inhibitors, notwithstanding its structural analogy with this class of drugs. To further add to the discrepancy, we found that both NAMPT inhibitors FK866 and GMX1778 entirely prevented initial NAD depletion in Vacor-exposed cells (Figure 2H). This finding prompted us to carefully evaluate the impact of Vacor on the two enzymes of the metabolic nicotinamide salvage pathway.

Vacor Is an Enzymatic Substrate of NAMPT

Disregarding the different kinetics of NAD depletion between Vacor and the two prototypical NAMPT inhibitors, the apparently paradoxical finding that FK866 and GMX1778 counteracted Vacor-dependent NAD drop further suggested an interaction between Vacor and NAMPT. We therefore first evaluated the effects of Vacor on recombinant human NAMPT activity and found that the chemical indeed inhibited the enzyme with an IC_{50} of 400 ± 28 nM (Figure 3A). This finding, together with the notion that compounds undergoing phosphoribosylation cause potent NAMPT inhibition (Sampath et al., 2015), prompted us to verify whether NAMPT can use Vacor as a substrate. We therefore incubated the recombinant human enzyme in the presence of PRPP, Vacor, and ATP and found, by means of high=performance liquid chromatography (HPLC) analysis, a time-dependent formation of a reaction product (Figure 3B). The formation of the product was dependent on the presence of PRPP (Figure S3A), suggesting its identity as phosphoribosyl Vacor (VMN). This assumption was confirmed by liquid chromatography-mass spectrometry (LC-MS) analysis of the incubated enzymatic mixture containing Vacor, which revealed the formation of a molecule with a molecular mass identical to that of VMN (Figure 3C). Interestingly, although in the NAMPT-catalyzed reaction NMN synthesis is coupled to a facultative ATP hydrolysis that causes a 6-fold increase of the k_{cat} for NMN synthesis (Burgos and Schramm, 2008), we found that NAMPT had the same activity toward Vacor in the presence or absence of ATP (Figure 3Bc). Still, V_{max} of VMN formation was comparable with that of NMN (28 ± 3 nmol/min/mg versus 30 ± 2 nmol/min/mg). The apparent K_M for Vacor was lower than the sensitivity threshold of our HPLC assay (i.e., lower than 2 μM), so we were not able to make a comparison with the K_M for nicotinamide, which is in the nanomolar range (Burgos and Schramm, 2008). Still, the finding that Vacor inhibits NAMPT activity with IC_{50} values in the nanomolar range when nicotinamide is present at 200 nM (see STAR Methods), a concentration very close to the K_M value, strongly suggests that the enzyme might use Vacor and nicotinamide with a comparable catalytic efficiency. Although the very low K_M value of NAMPT for nicotinamide precluded a deeper analysis of the Vacor inhibition mechanism, we were able to analyze the inhibition mechanism with respect to PRPP. In line with prior work (Burgos and Schramm, 2008), we found a K_M value for PRPP of 5 ± 2.0 μM. Under this condition, Vacor behaved as a competitive inhibitor with a K_i of 1.56 ± 0.8 μM (Figure S3B). Next, a docking study was undertaken to gather information on the molecular interactions between NAMPT and Vacor. To this end, we used the 3D coordinates of human NAMPT (PDB: 4L4L, high resolution of 2.12 Å) cocrystallized with the phosphoribosylated inhibitor 6-({4-[(3,5-difluorophenyl)sulfonyl]benzyl}carbamoyl)-1-(5-O-phosphono-β-D-ribofuranosyl)imidazo[1,2-a]pyridin-1-ium (Oh et al., 2014). Remarkably, when Vacor and VMN were docked in the catalytic pocket of human NAMPT, their best putative candidate positions were similar to that of the prototypical NAMPT inhibitor FK866 (Figure 3D). In particular, we found that the pyridyl ring of Vacor makes two π-π interactions with aromatic amino acids Tyr18 and Phe193, and that hydrogen bonds are possible between Vacor ureidic group and Asp219 (Figure S3C). Importantly, we also found that the pyridyl moiety of Vacor may acquire a peculiar binding position similar to that of the imidazole ring of the above cocrystallized inhibitor (Oh et al., 2014) (Figures 3E and S3D), thereby corroborating LC-MS data showing phosphoribose condensation with Vacor. As discovered in other crystals (PDB: 2E5C and 2E5D), this binding mode is also similar of that of the natural substrate nicotinamide and close to the binding site for PRPP (Takahashi et al., 2010). These results taken together were consistent with HPLC and LC-MS data indicating that Vacor can behave as an NAMPT substrate, undergoing phosphoribosylation to form VMN and cause enzymatic inhibition.

Metabolic Adenylation of VMN Leads to the Synthesis of the NAD Analog VAD

We then reasoned that the sole conversion of Vacor into VMN could not entirely explain its ability to rapidly induce NAD depletion and cell death. Indeed, even GMX1778 is phosphoribosylated by NAMPT but, although it was among those that most efficiently reduce cellular NAD content (Beauparlant et al., 2009), it appeared much less active than Vacor in depleting NAD contents and triggering cell death (see Figures 2F and S2C). Furthermore, the ability of NMN to fully prevent NAD depletion by FK866 or GMX1778 but not by Vacor was a clear hint that NAMPT inhibition is not the sole mechanism responsible for Vacor-dependent dinucleotide shortage and cell killing. We therefore hypothesized that Vacor and/or VMN also target the metabolic step of NAD resynthesis downstream of phosphoribosylation, namely the adenylation reaction brought about by NMNAT1–3 (Berger et al., 2005). We found that Vacor up to 400 nM did not affect the activity of NMNAT1–3 (data not shown), whereas a reaction product appeared when NMNAT2 or NMNAT3 was assayed with VMN and ATP as substrates (Figure 4A). To our surprise, LC-MS analysis of the corresponding HPLC peak demonstrated that it corresponded to VAD (Figure 4B). When compared with the adenylation reaction with NMN as substrate, adenylation of VMN by NMNAT2 and NMNAT3 was 0.6% ± 0.08% and 0.04% ± 0.006%, respectively.

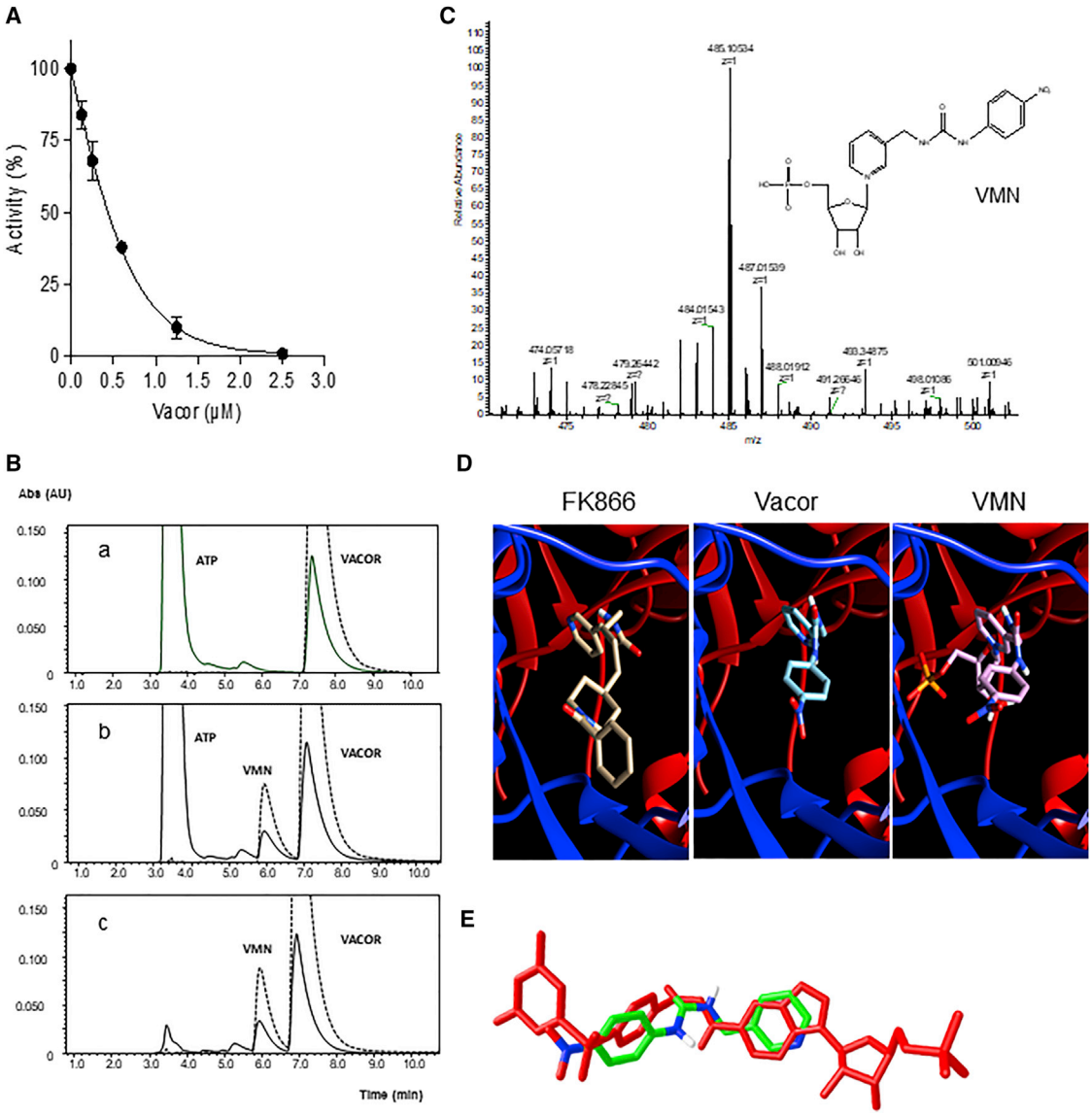

Figure 3. Vacor Is Metabolized into VMN by NAMPT

(A) Effect of Vacor on activity of human recombinant NAMPT. Each point is the SEM of 3 experiments conducted in duplicate.

(B) HPLC profiles at 260 nm (solid line) and 340 nm (dotted line) of hNAMPT reaction mixtures containing 0.4 mM Vacor, 1 mM PRPP, and 3.0 mU/mL hNAMPT, after 0 (a) and 60 min incubation at 37°C in the presence (b) and in the absence (c) of 1 mM ATP.

(C) Mass spectrometry spectrum of VMN.

(D) Docking pose of FK866, Vacor, and VMN in the catalytic binding site of human NAMPT.

(E) Docking of the best binding mode of Vacor (stick rendering, colors by element type) with the pose of the cocrystallized (6-({4-[(3,5-difluorophenyl)sulfonyl] benzyl}carbamoyl)-1-(5-O-phosphono-β-D-ribofuranosyl)imidazo[1,2-a]pyridin-1-ium) (red color) in the hNAMPT binding site.

Kinetic analysis of the NMNAT2-catalyzed reactions showed that affinity for VMN was 10-fold lower than that for NMN, whereas catalytic efficiency of VAD formation was about 2,000–fold lower than that of NAD (Figure 4C). We also tested VAD against the three recombinant human NMNATs and found that it had no effects on NMNAT1, whereas it inhibited NMNAT2 and NMNAT3 with IC_{50}s of 20 ± 2 μM and 463 ± 99 μM, respectively (Figure 4D).

On this basis, to determine the VAD binding site on hNMNAT2 we took advantage of comparative modeling, since no crystal structures are available. By using docking studies, we found that VAD can fit a putative binding pocket (Figure 4E) similar to that reported for NAD cocrystallized in NMNAT1 (PDB: 1KQN [Zhou et al., 2002]), making a net of hydrogen bonds with the side chain of His24, Tyr50, and Ser265 and with the backbone of Ile9, Leu207, and Asn209 (Figure S3E). Of note, His24 is known to be crucial for enzymatic activity (Yalowitz et al., 2004). Structural comparison between our new model of hNMNAT2 and the chain A of crystallized hNMNAT1 (Zhou et al., 2002) and NMNAT3 (Zhang et al., 2003) was then

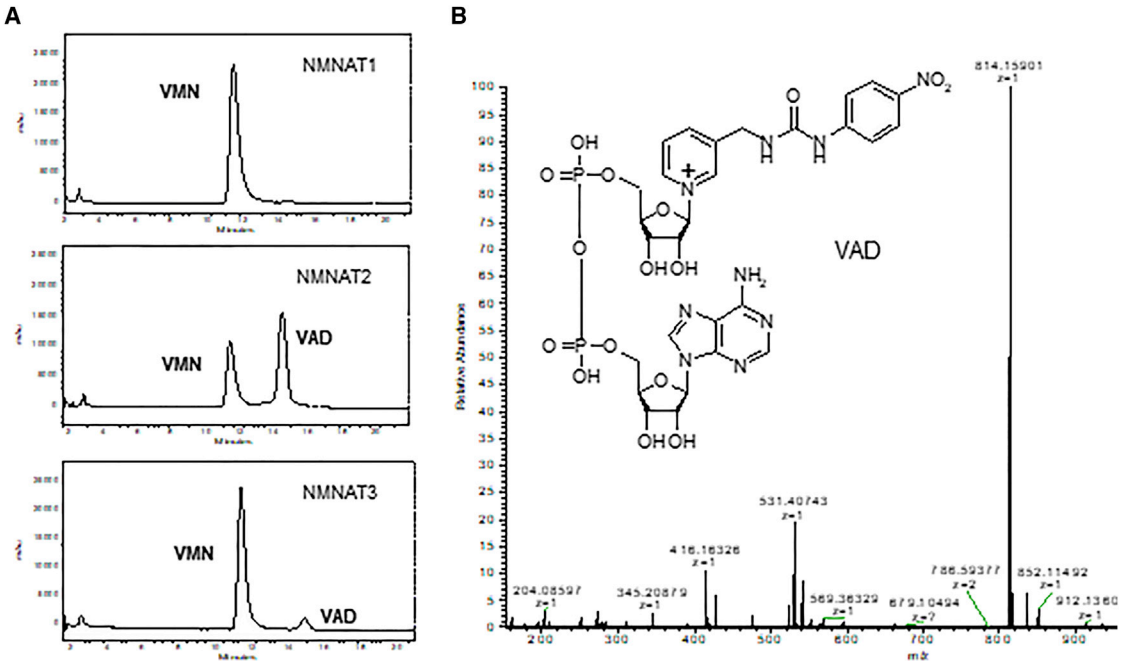

C

	K_m (μM)	V_{max} (mU/ml)	V_{max}/K_m
VMN	288±24	4.2±0.8	0.015
NMN	22±1.9	700±30	32

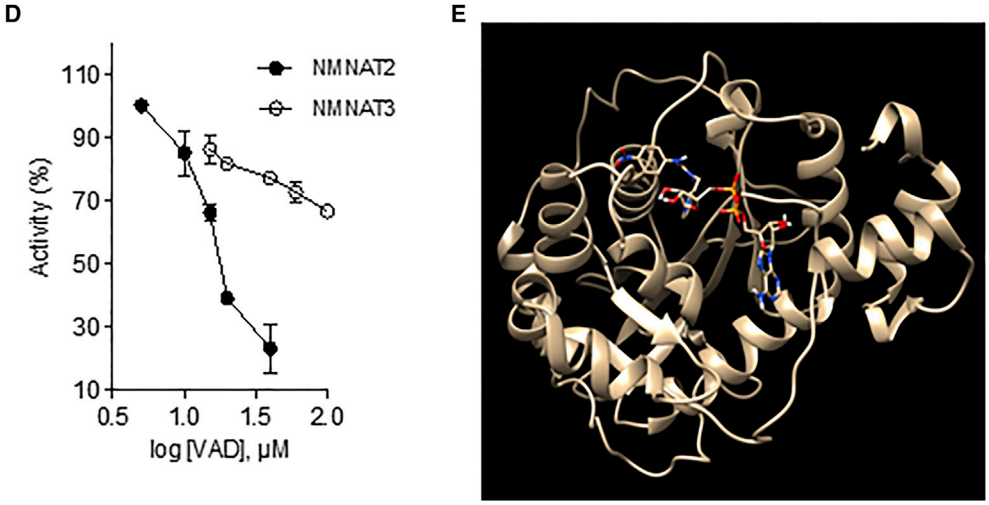

Figure 4. VMN Is Transformed into VAD by NMNAT2

(A) HPLC profiles at 340 nm of the NMNAT reaction mixtures prepared as described in STAR Methods.

(B) Mass spectrometry spectrum of VAD.

(C) Kinetic analysis of the VAD- and NAD-synthesizing activity of hNMNAT2 performed as described in STAR Methods.

(D) Effect of VAD on activity of human recombinant NMNAT2 and NMNAT3.

(E) VAD best docking candidate position (stick rendering, colors by element type) in the model of hNMNAT2 (cartoon rendered).

In (C) and (D), each value/point is the mean ± SEM of 3 (C) and 2 (D) experiments conducted in duplicate.

performed by the superimposition of the corresponding 3D structures. As highlighted in Figure S4A, a sequence not aligned with NMNAT2 or NMNAT3 is present at the C terminus of NMNAT1 that bends over the substrate binding site. Possibly, therefore, this sequence of 16 amino acids (DRNAGVILA PLQRNTA) can interact with the catalytic site, thereby regulating substrate entry or enzyme activity. Of note, the last seven amino acids of this terminal sequence can make direct interactions with the side chain of docked VAD. These results taken together may in part explain selective inhibition of NMNAT2 and NMNAT3, but not of NMNAT1, by VAD formation.

We next investigated the effect of VMN on the NAD-synthesizing activity of NMNAT2 at varying NMN concentrations and at a fixed, saturating ATP concentration. The resulting Lineweaver-Burk plot was consistent with a mixed-type inhibition (Figure S4B). Replots of slopes and intercepts against inhibitor concentrations generated concave-up curves (Figure S4B), indicating a multiple-site inhibition mechanism by VMN characterized by a concomitant binding of more than one inhibitor molecule (Segel, 1993). By analyzing the best fitting of the experimental initial rates (see equation in STAR Methods), we found a K_M for NMN of 14 ± 6 μM, a K_i of VMN for the free enzyme of 203 ± 25 μM, and a slightly higher K_i of VMN for the enzyme-substrate (ES) complex (αK_i 244 ± 30 μM). The kinetic model of inhibition is shown in Figure S4C.

In principle, given the low catalytic efficiency of NMNAT2 with VMN as substrate, under homeostatic conditions adenylation of NMN should outcompete that of VMN. We therefore investigated whether metabolic transformation of Vacor into VAD occurs in intact cells. Remarkably, a time-dependent increase of VMN and VAD was observed in Vacor-sensitive SH-SY5Y cells, whereas low content of VMN and no VAD was observed in Vacor-insensitive HeLa cells (Figure 5A). Interestingly, we found that VMN content was higher and VAD content was lower in M26C cells than in SH-SY5Y cells (Figure S5A) in keeping with the lower sensitivity to Vacor of the former compared with the latter (Figure S5B). We also found that Vacor prompted a rapid drop in NMN that preceded that of NAD in SH-SY5Y cells, whereas it had no effects on NMN and NAD in HeLa cells (Figure 5B). We reason that in Vacor-exposed cells the rapid drop in NMN content due to NAMPT inhibition by VMN allows VMN adenylation and VAD formation, notwithstanding the lower k_{cat} of NMNAT2 with VMN than with NMN as substrate. Together, these findings corroborated the hypothesis that a key determinant of Vacor cytotoxicity is its two-step metabolic conversion into VAD by NAMPT and NMNAT2. Two additional experiments strengthened this assumption. First, sensitivity to Vacor was associated with a high degree of NMNAT2 but not NMNAT1 expression levels (Figures 5C, 5D, S5C, and S5D). Second, VAD displayed identical cytotoxic effects when added to the medium of SH-SY5Y and HeLa cells (Figure 5E), also suggesting intracellular VAD entrance. To rule out a possible extracellular hydrolysis of VAD akin to NAD (Kulikova et al., 2015), we checked by means of LC-MS for the presence of extracellular VMN or NMN in HeLa cell cultures exposed for 1 hr to VAD or NAD (both at 1 mM), respectively. Upon incubation, we found that extracellular NMN increased from 2 ± 1.7 to 9.4 ± 1.2 nmol/mL, whereas VMN was not detectable.

Metabolic Conversion of Vacor Impairs Dehydrogenase Activity and Glycolysis, and Triggers Necrosis

Given the structural analogy between VAD and NAD, the former could compromise NAD-dependent enzymes behaving as a sort of false metabolic cofactor, similarly to tiazofurin (Chen and Pankiewicz, 2007). As a proof of concept we investigated the effects of VAD on two NAD-dependent dehydrogenases, namely inosine monophosphate dehydrogenase (IMPDH) and glyceraldehyde 3-phosphate dehydrogenase (GA3PDH). Remarkably, VAD inhibited both enzymes in a dose-dependent manner (Figure 5F), showing IC_{50}s of 52.2 ± 6 μM and 120 ± 21 μM on IMPDH and GA3PDH, respectively. We also analyzed the type of GA3PDH inhibition by VAD. The Lineweaver-Burk plots and their slopes and intercepts were consistent with a linear mixed-type inhibition (Figure S5E). The K_i value of VAD for the free enzyme was 85 ± 7 μM, which is only about 3-fold higher than the K_M value for NAD (28 ± 8 μM). The K_i of VAD for the ES complex (αK_i) was 29 ± 10 μM, indicating that the inhibitor shows a 3-fold greater affinity for the complex than for the free enzyme. Evidence of VAD-dependent GA3PDH inhibition, together with the concomitant shortage of its cofactor NAD, suggested that glycolysis is severely compromised in Vacor-exposed cells. Accordingly, the glycolytic end product lactate, the Krebs cycle by-product CO_2, and cellular ATP were all reduced time-dependently upon Vacor exposure (Figure 5G). We next wondered what type of cell death is triggered by Vacor, in light of its unique ability to prompt concomitant targeting of NAMPT and NMNAT2, rapid NAD and ATP depletion, inhibition of dehydrogenases, and, theoretically, additional NAD-dependent enzymes. We found that temporal kinetics of cell demise caused by Vacor were identical to those displayed by the prototypical necrotic inducer Na-azide, whereas those of the apoptotic trigger staurosporine were much delayed (Figure 5H). Furthermore, Hoechst staining demonstrated that nuclei of cells exposed to Vacor underwent pyknosis similar to those of cells exposed to Na-azide and did not display nuclear fragmentation typically triggered by staurosporine (Figure 5I). These findings, along with evidence of early propidium iodide positivity in Vacor-exposed cells (see Figure 2A), indicated that necrosis occurs as a result of Vacor toxification into VAD.

Tumoricidal Activity of Vacor Metabolism *In Vivo*

In light of the cytotoxic effects of Vacor *in vitro*, we next evaluated its tumoricidal potential *in vivo*. We found that Vacor injected intraperitoneally (i.p.) at 40 mg/kg every 4 days starting when tumor was palpable (i.e., around 0.1 cm^3) significantly reduced the growth of neuroblastoma xenografts in nude mice (Figure 6A). We next asked whether even a delayed treatment with Vacor could counteract tumor growth. To answer this question, we treated neuroblastoma-injected nude mice when the tumor volume reached 0.5 cm^3 with daily Vacor injections of 20 mg/kg i.p. and found that this treatment schedule also reduced tumor growth (Figure 6B). Remarkably, Vacor also delayed the growth of melanoma xenografts when dosed at 40 mg/kg every 4 days starting when xenografts were palpable (Figure 6C). At this dosage, Vacor did not alter mouse weight or blood glucose (Figure S6). Interestingly, NMNAT2 expression levels increased in both neuroblastoma and

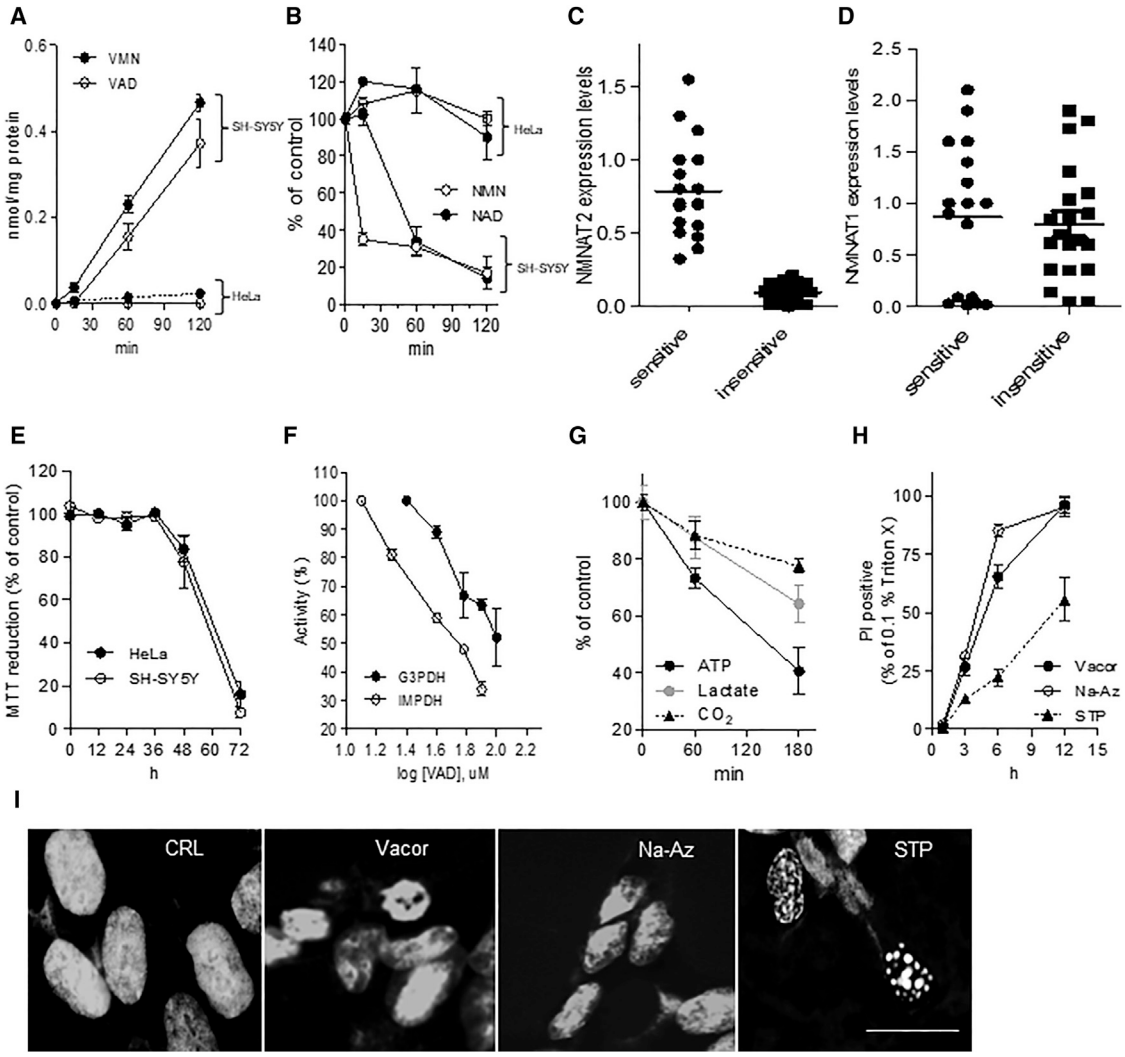

Figure 5. Effects of VAD on Dehydrogenase Activity and Cell Survival

(A) Intracellular content of VMN and VAD in SH-SY5Y or HeLa cells exposed to 100 μM Vacor.

(B) Intracellular content of NMN and NAD in SH-SY5Y or HeLa cells exposed to 100 μM Vacor.

(C and D) Expression levels of NMNAT2 (C) and NMNAT1 (D) in Vacor-sensitive and Vacor-insensitive cells.

(E) Effect of VAD (100 μM) addition to the culture medium on viability of SH-SY5Y and HeLa cells.

(F) Effect of VAD on activity of human recombinant GA3PDH and IMPDH.

(G) Temporal kinetics of the effect of Vacor (100 μM) on intracellular lactate and ATP content, as well as CO_2 production by SH-SY5Y cells.

(H) Time course of cell death in cultures exposed to Vacor (100 μM), NaAz (1 mM), and staurosporine (300 nM).

(I) Hoechst staining of cells exposed for 3 hr to Vacor (100 μM), NaAz (1 mM), and staurosporine (300 nM). Scale bar, 10 μm.

In (C) and (D), points represent values of single PCR analysis. In the other figures, each point/bar represents the mean ± SEM of at least 3 experiments.

melanoma xenografts, returning to levels originally found in cell cultures 10 days after reseeding from xenograft (Figure 6D). Although mechanisms responsible for increased expression of NMNAT2 within xenografts are currently unknown, we speculate that they can be in part related to increased activity of NMNAT2 promoter due to signaling occurring in the tumor microenvironment.

Next, to gather information on Vacor metabolism in tumors, we quantified its content as well as that of VAD in neuroblastoma xenografts of nude mice challenged for 5 days with Vacor (20 mg/kg, i.p.). We found that both Vacor and VAD were present in the tumor mass at concentrations of 278 ± 35 and 2.83 ± 0.11 pmol/mg, respectively. To corroborate these findings we also took advantage of MS imaging of Vacor and adenine adenylates to localize their intratumoral distribution. Importantly, as shown in Figure 6E, we found that Vacor was detectable within the xenograft region of colliquative necrosis, and colocalized with AMP (a typical marker of necrotic tissue) but not with ATP (a marker of healthy tissue). No signal was obtained for VMN and VAD, suggesting that their contents were below detection limits of MS imaging. Evidence that Vacor accumulates in the necrotic but not viable xenograft region corroborates HPLC data showing metabolic Vacor transformation by the neoplastic tissue *in vivo*.

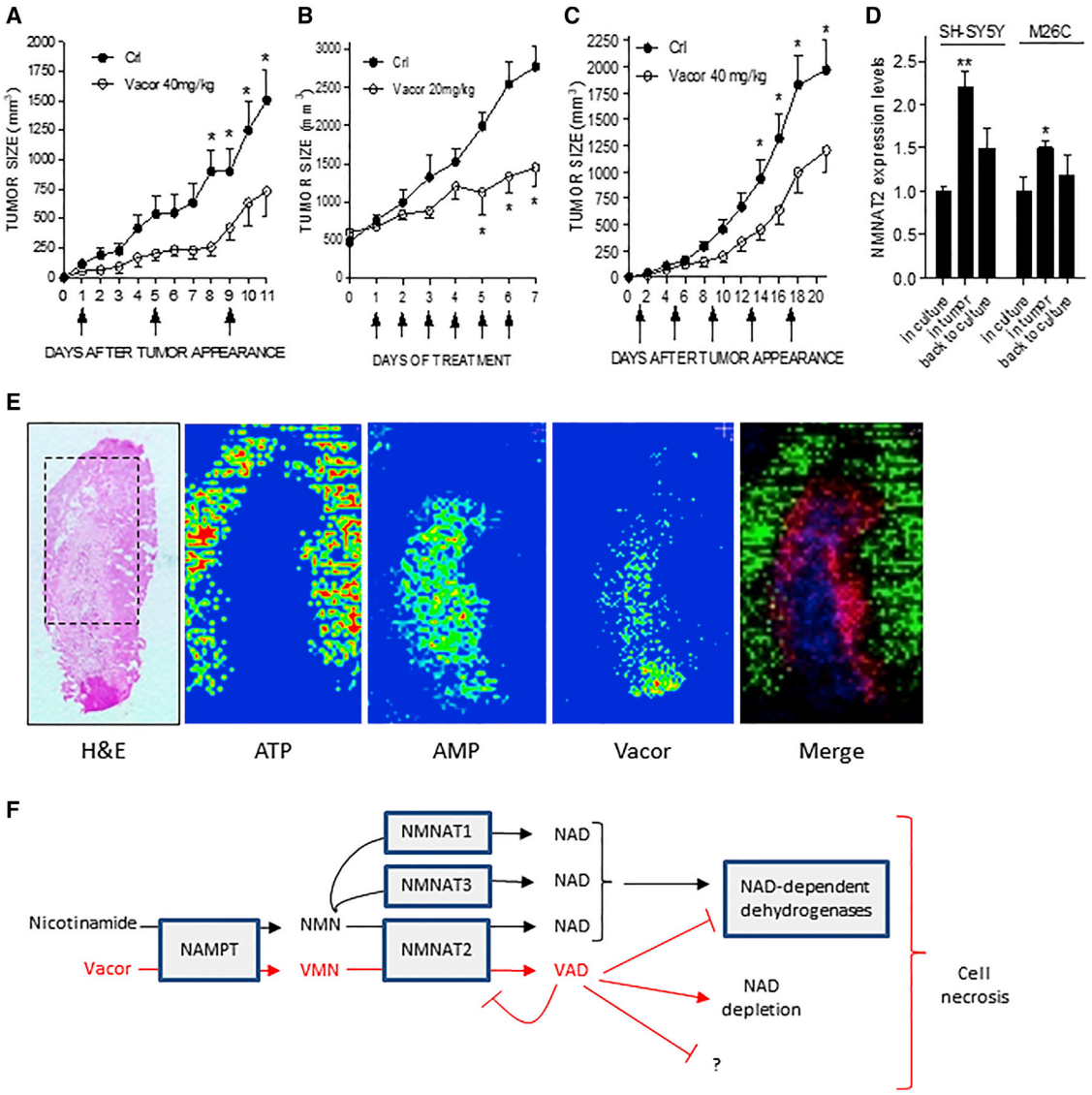

Figure 6. Vacor Reduces Growth of Neuroblastoma and Melanoma Xenografts

(A) Temporal kinetics of SH-SY5Y xenograft growth in nude mice (12 female mice per group) receiving intraperitoneal injections of vehicle (DMSO) or Vacor (40 mg/kg) every 4 days starting when tumor was palpable (around 0.1 cm^3).

(B) Temporal kinetics of SH-SY5Y xenograft growth in nude mice (5 female mice per group) receiving daily intraperitoneal injections of vehicle (DMSO) or Vacor (20 mg/kg) starting at tumor volumes of 0.5 cm^3.

(C) Temporal kinetics of melanoma M26C xenograft growth in nude mice (14 female mice per group) receiving intraperitoneal injections of vehicle (DMSO) or Vacor (40 mg/kg) every 4 days starting when tumor was palpable.

(D) NMNAT2 transcript levels in SH-SY5Y neuroblastoma or M26C melanoma cells in cultures, in xenografts, and back in cultures for 7 days.

(E) H&E staining of an SH-SY5Y xenograft section showing the external viable cortex and internal necrotic core. Inset relates to the region that has been analyzed by mass spectrometric imaging for tissue distribution of ATP, AMP, and Vacor.

(F) Metabolic pathway of Vacor toxification.

In (A), (B), and (C), *$p < 0.05$ versus control (Crl) by Student's t test. In (D), **$p < 0.01$ versus "in culture" and "back to culture" by ANOVA and Tukey's post hoc test.

DISCUSSION

The present study originally demonstrates that the nicotinamide salvage pathway can operate as a toxification route for the synthesis of new antimetabolites with pleiotypic effects on cell metabolism. Specifically, we provide evidence that the coordinated action of NAMPT and NMNAT2 transforms Vacor into a mimetic of NAD and its precursors, thereby triggering rapid derangement of the NAD metabolome. Of note, this new toxification route (Figure 6F) prompts necrosis of specific tumor cell types and also exerts tumoricidal activity *in vivo*.

Current NAMPT inhibitors that reached the clinical arena typically trigger slow (24–48 hr) NAD depletion (Sampath et al., 2015; Shackelford et al., 2013), and it is unknown

whether these delayed kinetics are due to slow intracellular NAD consumption rates and/or to the ability of alternative NAD biosynthetic pathways, such as those converging on NMNAT from NR, nicotinic acid, and quinolinic acid to circumvent the NAMPT block and sustain NAD formation. Our data show that concomitant inhibition of NAMPT and NMNAT prompts immediate NAD depletion, indicating for the first time that, at least in certain tumor cells, NAD turnover is extraordinarily rapid, and metabolic pathways different from that rescuing nicotinamide are functionally relevant to NAD biosynthesis. Also, preservation of mitochondrial NAD at early time points in cells undergoing massive NAD depletion further corroborates prior evidence that mitochondrial NAD metabolism is functionally independent of that occurring within the cytoplasm (Pittelli et al., 2010). Of note, data showing the ability of NMNAT2 to transform VMN into VAD and undergo product inhibition are also of relevance to NAD enzymology. Furthermore, selectivity of VAD toward NMNAT2 inhibition provides information of relevance to the understanding of NMNAT2 structure and catalysis, as well as to development of potent and selective NMNAT inhibitors with antineoplastic potential.

At present we do not know how relevant the possible inhibition of each NAD-dependent enzyme is to the metabolic derangement induced by Vacor. Inevitably, profiling the sensitivity of NAD dehydrogenases and NAD-hydrolyzing enzymes to VAD-like antimetabolites needs additional work. Still, given the central role of aerobic glycolysis in tumor growth and progression (Deberardinis and Chandel, 2016), the ability of VAD to inhibit the key glycolytic enzyme GAPDH underscores the relevance of Vacor and possible analogs as innovative antimetabolites for tumor therapy. In this regard two main points, namely tumor selectivity and drug tolerability, still need to be addressed. As for tumor selectivity, although Vacor-like drugs may appear selective for neoplasms expressing NMNAT2 (that might become a biomarker of sensitivity), future chemicals designed to be transformed by NMNAT1 or NMNAT3 may have a different spectrum of activity. As far as the tolerability of Vacor-like antimetabolites is concerned, in light of the specific roles played by NAD in metabolic homeostasis of different tissues (Lin et al., 2016; Mills et al., 2016; Verdin, 2015), it will be important to understand whether pharmacological strategies able to minimize toxicity of NAMPT inhibitors, such as specific administration routes, treatment paradigms, and/or rescue agents (Roulston and Shore, 2016), can also reduce off-target toxicity of these double enzyme inhibitors. Furthermore, it is worth noting that even a partial metabolic impairment exerted by low, non-toxic doses of Vacor-like drugs might sensitize tumors to current chemotherapeutics. As a final note, it is worth mentioning that severe human intoxication due to ingestion of high doses of Vacor for suicide purposes are associated with development of peripheral neuropathy and diabetes mellitus, albeit via mechanisms that are currently unknown (Lewitt, 1980; Vogel, 1982). Our findings for the first time strongly suggest that tissue-selective depletion of the metabolic NAD pool underlies the pathogenesis of both disorders. In keeping with this hypothesis, NMNAT2 is highly expressed in neurons (Conforti et al., 2014) and β cells (Yalowitz et al., 2004). More intriguingly, derangement of NAD biosynthesis is of pathogenetic relevance to the development of both axonal degeneration (Conforti et al., 2014) and diabetes mellitus (Revollo et al., 2007; Yoshino et al., 2011). This reasoning sheds new light on the key role of the nicotinamide salvage pathway in human disorders whose pathogenesis is as yet unknown. For instance, NAD depletion and ensuing metabolic derangement may concur with the pathogenesis of neuropathies typically occurring in patients on chronic therapies with pyridine ring-containing drugs such as isoniazid or bortezomib.

Overall, our study provides the rationale to harness the two enzymes of the metabolic route of nicotinamide salvage as a new toxification pathway to generate pyridine antimetabolites. Further studies might identify more potent Vacor derivatives with different degrees of selectivity toward NMNATs and human neoplasms. At the same time, however, these antimetabolites may also help to further our understanding of the complex homeostasis of NAD metabolism in different tissues, and its relevance to pathogenesis and the treatment of human disorders.

SIGNIFICANCE

A large body of evidence indicates that specific metabolic alterations occur in different types of tumors, and there is great interest in designing chemicals able to target these alterations for therapeutic purposes. Recently, much effort has been directed at identifying molecules able to interfere with the NAD metabolome in light of the notion that NAD consumption is increased in cancer cells, which, therefore, should be sensitized to chemicals able to deplete intracellular NAD contents. Only two enzymes, namely nicotinamide phosphoribosyl transferase (NAMPT) and nicotinamide mononucleotide adenylyl transferase (NMNAT1-3) operate in the nicotinamide salvage pathway, a central route able to resynthesize NAD from nicotinamide. Several potent NAMPT inhibitors have been developed but have failed in clinical trials for treatment of different tumors because additional NAD-synthesizing pathways circumvent the NAMPT block and directly converge on NMNAT, allowing NAD synthesis. Unfortunately, no NMNAT inhibitors have been yet identified. In this study we screened chemicals bearing the ureidic-pyrimidine group as new NAMPT inhibitors. Unexpectedly, we identified a compound known as Vacor, previously used as a rodenticide, as a new structure able to be transformed by both NAMPT and NMNAT2 into antimetabolites with antineoplastic potential. Specifically, Vacor is phosphoribosylated by NAMPT into Vacor mononucleotide, which is then adenylated into Vacor adenine dinucleotide (VAD), a NAD analog. Notably, this intracellular chemical transformation causes concomitant inhibition of both NAMPT and NMNAT with unprecedented rapid NAD depletion, as well as inhibition by VAD of NAD-dependent enzymes such as dehydrogenases. These biochemical events, in turn, prompt bioenergetic derangement and necrosis only of those NMNAT2-expressing cancer cells and tumor xenografts able to metabolize Vacor into VAD. For the first time our study identifies the entire nicotinamide salvage pathway as a new toxification route for innovative antineoplastic chemicals.

STAR★METHODS

Detailed methods are provided in the online version of this paper and include the following:

- KEY RESOURCES TABLE
- CONTACT FOR REAGENT AND RESOURCE SHARING
- EXPERIMENTAL MODEL AND SUBJECT DETAILS
  - Cell Culture
  - *In vivo* Tumor Xenograft Model
- METHOD DETAILS
  - NAD, NADH and ATP Measurement
  - Evaluation of Mitochondrial Membrane Potential
  - Cell Fractionation
  - Oxygen Consumption Analysis
  - Lactate Assay
  - Radioactive Metabolic Assay
  - Preparation of Human Recombinant NAMPT and NMNATs
  - Preparation of VMN and VAD
  - Kinetic and Inhibition Studies on NAMPT and NMNATs
  - Effect of VAD on Dehydrogenases Activity
  - Determination of Nucleotides and Vacor Metabolites in Cell Lysates
  - Molecular Modeling
  - RNA Isolation and qPCR
  - MS Imaging
  - ESI- HRMS Electrospray High Resolution Mass Spectrometry
- QUANTIFICATION AND STATISTICAL ANALYSIS
- DATA AND SOFTWARE AVAILABILITY

SUPPLEMENTAL INFORMATION

Supplemental Information includes six figures and one table and can be found with this article online at https://doi.org/10.1016/j.chembiol.2018.01.012.

ACKNOWLEDGMENTS

This work was supported by grants from the Italian Foundation for Multiple Sclerosis 2014/R/6, Regione Toscana Rare Disease Projects Heath Projects 2007 and 2009, Ente Cassa di Risparmio di Firenze (ECRF 2015.0964), Italian Ministry of Health, research grant GR-2011-02352225, and Associazione Italiana per la Ricerca sul Cancro AIRC IG-2017-20451.

AUTHOR CONTRIBUTIONS

A.C., D.B., M.Z., and N.R. designed the experiments; D.B., F.R., and G.R. carried out *in vitro* experiments; F.M., F.Z., C.D., and N.R. carried out biochemical experiments and HPLC analysis; D.B., G.R., B.S., and M.M. carried out xenograft experiments; E.C. carried out chemistry computational/modeling; R.Z., G.P., M.C., and G.B. carried out mass spectrometry analyses; A.C. and N.R. wrote the paper. All authors reviewed the manuscript.

DECLARATION OF INTERESTS

The authors declare no competing interests.

Received: June 6, 2017
Revised: October 23, 2017
Accepted: January 26, 2018
Published: February 22, 2018

REFERENCES

Balducci, E., Emanuelli, M., Raffaelli, N., Ruggieri, S., Amici, A., Magni, G., Orsomando, G., Polzonetti, V., and Natalini, P. (1995). Assay methods for nicotinamide mononucleotide adenylyltransferase of wide applicability. Anal. Biochem. *228*, 64–68.

Beauparlant, P., Bedard, D., Bernier, C., Chan, H., Gilbert, K., Goulet, D., Gratton, M.O., Lavoie, M., Roulston, A., Turcotte, E., et al. (2009). Preclinical development of the nicotinamide phosphoribosyl transferase inhibitor prodrug GMX1777. Anticancer Drugs *20*, 346–354.

Berger, F., Lau, C., Dahlmann, M., and Ziegler, M. (2005). Subcellular compartmentation and differential catalytic properties of the three human nicotinamide mononucleotide adenylyltransferase isoforms. J. Biol. Chem. *280*, 36334–36341.

Bieganowski, P., and Brenner, C. (2004). Discoveries of nicotinamide riboside as a nutrient and conserved NRK genes establish a Preiss-Handler independent route to NAD+ in fungi and humans. Cell *117*, 495–502.

Bogan, K.L., and Brenner, C. (2008). Nicotinic acid, nicotinamide, and nicotinamide riboside: a molecular evaluation of NAD+ precursor vitamins in human nutrition. Annu. Rev. Nutr. *28*, 115–130.

Boroughs, L.K., and Deberardinis, R.J. (2015). Metabolic pathways promoting cancer cell survival and growth. Nat. Cell Biol. *17*, 351–359.

Brunetti, L., Di Stefano, M., Ruggieri, S., Cimadamore, F., and Magni, G. (2010). Homology modeling and deletion mutants of human nicotinamide mononucleotide adenylyltransferase isozyme 2: new insights on structure and function relationship. Protein Sci. *19*, 2440–2450.

Burgos, E.S., and Schramm, V.L. (2008). Weak coupling of ATP hydrolysis to the chemical equilibrium of human nicotinamide phosphoribosyltransferase. Biochemistry *47*, 11086–11096.

Canto, C., Menzies, K.J., and Auwerx, J. (2015). NAD(+) metabolism and the control of energy homeostasis: a balancing act between mitochondria and the nucleus. Cell Metab. *22*, 31–53.

Chen, L., and Pankiewicz, K.W. (2007). Recent development of IMP dehydrogenase inhibitors for the treatment of cancer. Curr. Opin. Drug Discov. Devel. *10*, 403–412.

Chiarugi, A. (2002). PARP-1: killer or conspirator? The suicide hypothesis revisited. Trends Pharmacol. Sci. *23*, 122–129.

Chiarugi, A., Dolle, C., Felici, R., and Ziegler, M. (2012). The NAD metabolome—a key determinant of cancer cell biology. Nat. Rev. Cancer *12*, 741–752.

Cipriani, G., Rapizzi, E., Vannacci, A., Rizzuto, R., Moroni, F., and Chiarugi, A. (2005). Nuclear poly(ADP-ribose) polymerase-1 rapidly triggers mitochondrial dysfunction. J. Biol. Chem. *280*, 17227–17234.

Conforti, L., Gilley, J., and Coleman, M.P. (2014). Wallerian degeneration: an emerging axon death pathway linking injury and disease. Nat. Rev. Neurosci. *15*, 394–409.

Deberardinis, R.J., and Chandel, N.S. (2016). Fundamentals of cancer metabolism. Sci. Adv. *2*, e1600200.

Formentini, L., Macchiarulo, A., Cipriani, G., Camaioni, E., Rapizzi, E., Pellicciari, R., Moroni, F., and Chiarugi, A. (2009). Poly(ADP-ribose) catabolism triggers AMP-dependent mitochondrial energy failure. J. Biol. Chem. *284*, 17668–17676.

Galli, U., Travelli, C., Massarotti, A., Fakhfouri, G., Rahimian, R., Tron, G.C., and Genazzani, A.A. (2013). Medicinal chemistry of nicotinamide phosphoribosyltransferase (NAMPT) inhibitors. J. Med. Chem. *56*, 6279–6296.

Kulikova, V., Shabalin, K., Nerinovski, K., Dölle, C., Niere, M., Yakimov, A., Redpath, P., Khodorkovskiy, M., Migaud, M.E., Ziegler, M., and Nikiforov, A. (2015). Generation, release, and uptake of the NAD precursor nicotinic acid riboside by human cells. J. Biol. Chem. *290*, 27124–27137.

Laskowski, R.A., and Swindells, M.B. (2011). LigPlot+: multiple ligand-protein interaction diagrams for drug discovery. J. Chem. Inf. Model. *51*, 2778–2786.

Lewitt, P.A. (1980). The neurotoxicity of the rat poison vacor. A clinical study of 12 cases. N. Engl. J. Med. *302*, 73–77.

Lin, J.B., Kubota, S., Ban, N., Yoshida, M., Santeford, A., Sene, A., Nakamura, R., Zapata, N., Kubota, M., Tsubota, K., et al. (2016). NAMPT-mediated NAD(+) biosynthesis is essential for vision in mice. Cell Rep. *17*, 69–85.

Luthy, R., Bowie, J.U., and Eisenberg, D. (1992). Assessment of protein models with three-dimensional profiles. Nature *356*, 83–85.

Maldi, E., Travelli, C., Caldarelli, A., Agazzone, N., Cintura, S., Galli, U., Scatolini, M., Ostanao, P., Miglino, B., Chiorino, G., et al. (2013). Nicotinamide phosphoribosyltransferase (NAMPT) is over-expressed in melanoma lesions. Pigment Cell Melanoma Res. *26*, 144–146.

Mills, K.F., Yoshida, S., Stein, L.R., Grozio, A., Kubota, S., Sasaki, Y., Redpath, P., Migaud, M.E., Apte, R.S., Uchida, K., et al. (2016). Long-term administration of nicotinamide mononucleotide mitigates age-associated physiological decline in mice. Cell Metab. *24*, 795–806.

Mori, V., Amici, A., Mazzola, F., Di Stefano, M., Conforti, L., Magni, G., Ruggieri, S., Raffaelli, N., and Orsomando, G. (2014). Metabolic profiling of alternative NAD biosynthetic routes in mouse tissues. PLoS One *9*, e113939.

Oh, A., Ho, Y.C., Zak, M., Liu, Y., Chen, X., Yuen, P.W., Zheng, X., Liu, Y., Dragovich, P.S., and Wang, W. (2014). Structural and biochemical analyses of the catalysis and potency impact of inhibitor phosphoribosylation by human nicotinamide phosphoribosyltransferase. Chembiochem *15*, 1121–1130.

Pedretti, A., Villa, L., and Vistoli, G. (2004). VEGA—an open platform to develop chemo-bio-informatics applications, using plug-in architecture and script programming. J. Comput. Aided Mol. Des. *18*, 167–173.

Pettersen, E.F., Goddard, T.D., Huang, C.C., Couch, G.S., Greenblatt, D.M., Meng, E.C., and Ferrin, T.E. (2004). UCSF Chimera—a visualization system for exploratory research and analysis. J. Comput. Chem. *25*, 1605–1612.

Piacente, F., Caffa, I., Ravera, S., Sociali, G., Passalacqua, M., Vellone, V.G., Becherini, P., Reverberi, D., Monacelli, F., Ballestrero, A., et al. (2017). Nicotinic acid phosphoribosyltransferase regulates cancer cell metabolism, susceptibility to NAMPT inhibitors and DNA repair. Cancer Res. *77*, 3857–3869.

Pittelli, M., Formentini, L., Faraco, G., Lapucci, A., Rapizzi, E., Cialdai, F., Romano, G., Moneti, G., Moroni, F., and Chiarugi, A. (2010). Inhibition of nicotinamide phosphoribosyltransferase: cellular bioenergetics reveals a mitochondrial insensitive NAD pool. J. Biol. Chem. *285*, 34106–34114.

Revollo, J.R., Korner, A., Mills, K.F., Satoh, A., Wang, T., Garten, A., Dasgupta, B., Sasaki, Y., Wolberger, C., Townsend, R.R., et al. (2007). Nampt/PBEF/Visfatin regulates insulin secretion in beta cells as a systemic NAD biosynthetic enzyme. Cell Metab. *6*, 363–375.

Roulston, A., and Shore, G.C. (2016). New strategies to maximize therapeutic opportunities for NAMPT inhibitors in oncology. Mol. Cell Oncol. *3*, e1052180.

Roy, A., Kucukural, A., and Zhang, Y. (2010). I-TASSER: a unified platform for automated protein structure and function prediction. Nat. Protoc. *5*, 725–738.

Sampath, D., Zabka, T.S., Misner, D.L., O'Brien, T., and Dragovich, P.S. (2015). Inhibition of nicotinamide phosphoribosyltransferase (NAMPT) as a therapeutic strategy in cancer. Pharmacol. Ther. *151*, 16–31.

Santini, R., Pietrobono, S., Pandolfi, S., Montagnani, V., D'Amico, M., Penachioni, J.Y., Vinci, M.C., Borgognoni, L., and Stecca, B. (2014). SOX2 regulates self-renewal and tumorigenicity of human melanoma-initiating cells. Oncogene *33*, 4697–4708.

Segel, I.H. (1993). Enzyme Kinetics: Behavior and Analysis of Rapid Equilibrium and Steady-State Enzyme Systems (John Wiley and Sons).

Shackelford, R.E., Mayhall, K., Maxwell, N.M., Kandil, E., and Coppola, D. (2013). Nicotinamide phosphoribosyltransferase in malignancy: a review. Genes Cancer *4*, 447–456.

Sociali, G., Raffaghello, L., Magnone, M., Zamporlini, F., Emionite, L., Sturla, L., Bianchi, G., Vigliarolo, T., Nahimana, A., Nencioni, A., et al. (2016). Antitumor effect of combined NAMPT and CD73 inhibition in an ovarian cancer model. Oncotarget *7*, 2968–2984.

Sorci, L., Cimadamore, F., Scotti, S., Petrelli, R., Cappellacci, L., Franchetti, P., Orsomando, G., and Magni, G. (2007). Initial-rate kinetics of human NMN-adenylyltransferases: substrate and metal ion specificity, inhibition by products and multisubstrate analogues, and isozyme contributions to NAD^+ biosynthesis. Biochemistry *46*, 4912–4922.

Takahashi, R., Nakamura, S., Nakazawa, T., Minoura, K., Yoshida, T., Nishi, Y., Kobayashi, Y., and Ohkubo, T. (2010). Structure and reaction mechanism of human nicotinamide phosphoribosyltransferase. J. Biochem. *147*, 95–107.

Trott, O., and Olson, A.J. (2010). AutoDock Vina: improving the speed and accuracy of docking with a new scoring function, efficient optimization, and multithreading. J. Comput. Chem. *31*, 455–461.

Verdin, E. (2015). NAD(+) in aging, metabolism, and neurodegeneration. Science *350*, 1208–1213.

Vogel, R.P. (1982). Poisoning with vacor rodenticide. Arch. Pathol. Lab. Med. *106*, 153.

Yalowitz, Y.A., Xiao, S., Biju, M.P., Antony, A.C., Cummings, O.W., Deeg, M.A., and Jayaram, H.N. (2004). Characterization of human brain nicotinamide 5'-mononucleotide adenylyl transferase-2 and expression in human pancreas. Biochem. J. *377*, 317–326.

Yang, J., Yan, R., Roy, A., Xu, D., Poisson, J., and Zhang, Y. (2015). The I-TASSER Suite: protein structure and function prediction. Nat. Methods *12*, 7–8.

Yoshino, J., Mills, K.F., Yoon, M.J., and Imai, S. (2011). Nicotinamide mononucleotide, a key NAD(+) intermediate, treats the pathophysiology of diet- and age-induced diabetes in mice. Cell Metab. *14*, 528–536.

Zamporlini, F., Ruggieri, S., Mazzola, F., Amici, A., Orsomando, G., and Raffaelli, N. (2014). Novel assay for simultaneous measurement of pyridine mononucleotides synthesizing activities allows dissection of the NAD(+) biosynthetic machinery in mammalian cells. FEBS J. *281*, 5104–5119.

Zhang, X., Kurnasov, O.V., Karthikeyan, S., Grishin, N.V., Osterman, A.L., and Zhang, H. (2003). Structural characterization of a human cytosolic NMN/NaMN adenylyltransferase and implication in human NAD biosynthesis. J. Biol. Chem. *278*, 13503–13511.

Zhou, T., Kurnasov, O., Tomchick, D.R., Binns, D.D., Grishin, N.V., Marquez, V.E., Osterman, A.L., and Zhang, H. (2002). Structure of human nicotinamide/nicotinic acid mononucleotide adenylyltransferase. Basis for the dual substrate specificity and activation of the oncolytic agent tiazofurin. J. Biol. Chem. *277*, 13148–13154.

STAR★METHODS

KEY RESOURCES TABLE

REAGENT or RESOURCE	SOURCE	IDENTIFIER
Chemicals and Recombinant Proteins		
Dulbecco's Modified Eagle's Medium (DMEM)	Sigma-Aldrich	Cat#D6429
4',6-diamidino-2-phenylindole (DAPI)	Sigma-Aldrich	Cat#D9542
Fetal bovine serum (FBS)	Thermo Fisher	Cat#10500064
L-Glutamine	Sigma-Aldrich	Cat#G7513
Penicillin/streptomycin	Sigma-Aldrich	Cat#P0781
FK866	Sigma-Aldrich	Cat#F8557
GMX1778	Sigma-Aldrich	Cat#SML0646
3-(4,5-dimethylthiazol-2-yl)-2,5-diphenyltetrazolium (MTT)	Sigma-Aldrich	Cat#M5655
Propidium iodide (PI)	Sigma-Aldrich	Cat#P4170
Matrigel	3V CHIMICA S.r.l.	Cat#354234
NAD	Sigma-Aldrich	Cat#N3014
NADH	Sigma-Aldrich	Cat#N8129
ATP	Sigma-Aldrich	Cat#A2383
GLUCOSE [U-14C]	Perkin Elmer	Cat#NEC042V250UC
TMRE	Sigma-Aldrich	Cat#87917
FCCP	Sigma-Aldrich	Cat#C2920
Nicotinamide Mononucleotide (NMN)	Sigma-Aldrich	Cat#N3501
Nicotinamide Riboside (NR)	ChromaDex	Cat#ASB-00014314
Nicotinamide (NAM)	Sigma-Aldrich	Cat#72340
5-Phospho-D-ribose 1-diphosphate (PRPP)	Sigma-Aldrich	Cat#P8296
Inosine 5'-monophosphate	Sigma-Aldrich	Cat#57510
DL-Glyceraldehyde 3'-phosphate	Sigma-Aldrich	Cat#G5251
Trizol Reagent	ThermoFisher	Cat#15596026
iScript	BioRad	Cat#1708890
SYBR Green PCR kit	BioRad	Cat#1725271
Bovine Serum Albumin (BSA)	Sigma-Aldrich	Cat#A7906
Bovine Serum Albumin (BSA for cycling assay)	Sigma-Aldrich	Cat#A8531-1VL
Riboflavin 5′-monophosphate (FMN)	Sigma-Aldrich	Cat#F8399
Resazurin	Sigma-Aldrich	Cat#R7017
Isopropyl β-D-1-thiogalactopyranoside (IPTG)	Sigma-Aldrich	Cat#I6758
Tris(2-carboxyethyl)phosphine HCl (TCEP)	Sigma-Aldrich	Cat#75259
3-([3-Cholamidopropyl]dimethylammonio)-2-hydroxy-1-propanesulfonate (CHAPSO)	Sigma-Aldrich	Cat#C3649
DL-Dithiothreitol	Sigma-Aldrich	Cat#43819
Phenylmethanesulfonyl fluoride (PMSF)	Fluka	Cat#78830
Protease Inhibitor Cocktail	Sigma-Aldrich	Cat#P8849
Ampicillin	Sigma-Aldrich	Cat#A9518
Kanamycin	Sigma-Aldrich	Cat#K4000
HisTrap HP column	GE Healthcare	Cat#17-5247-01
PD-10 desalting columns (Sephadex G-25)	GE Healthcare	Cat#17-0851-01
PD MiniTrap (Sephadex)G-25	GE Healthcare	Cat#28-9180-07
Supelcosil LC-18-S HPLC column	Supelco (Sigma-Aldrich)	Cat#58928-U
Supelcosil LC-18-T HPLC column	Supelco (Sigma-Aldrich)	Cat#58971

(*Continued on next page*)

Continued

REAGENT or RESOURCE	SOURCE	IDENTIFIER
Kinetex 2.6 μm C18 100A	Phenomenex	Cat#00F-4462-E0
Kinetex 2.6 μm HILIC 100A	Phenomenex	Cat#00F-4461-E0
TRACER EXTRASIL ODS2 5 μm	Phenomenex	Cat#N34544
Glyceraldehyde-3-phosphate Dehydrogenase	Sigma-Aldrich	Cat#G9263
Inosine Monophosphate Dehydrogenase Type II human	Sigma-Aldrich	Cat#I1782
Diaphorase from Clostridium kluyveri	Sigma-Aldrich	Cat#D5540
pET15b vector	Novagen, EMD Millipore	Cat#69661-3
Recombinant Human NAMPT	This study	N/A
pTrcHisA- NMNAT1	Sorci et al., 2007	N/A
pET28c- NMNAT2	Brunetti et al., 2010	N/A
pTrcHisA- NMNAT3	Sorci et al., 2007	N/A
Recombinant E.coli NMN deamidase (PncC)	Zamporlini et al., 2014	N/A
Recombinant B. anthracis NaMN adenylyltransferase (NadD)	Zamporlini et al., 2014	N/A
Recombinant B. anthracis NAD synthetase (NadE)	Zamporlini et al., 2014	N/A
α-cyano-hydroxycynnamic acid	Sigma-Aldrich	Cat#C2020
Aniline	Sigma-Aldrich	Cat#51788
9-aminoacridine	Sigma-Aldrich	Cat#92817
Oligonucleotides		
Oligonucleotides used, see Table S1	This study	N/A
Bacterial strains		
One Shot BL21 Star (DE3) Chemically Competent E.coli cells	Invitrogen	Cat#440049
One Shot TOP 10 Chemically Competent E.coli cells	Invitrogen	Cat#404003
Critical Commercial Assays		
ATPlite Luminescence Assay	Perkin Elmer	Cat#6016943
Bradford Protein Assay	BioRad	Cat#5000201
Lactate assay kit	BioVision	Cat#K607
Human NMNAT2	This study	UniProtKB/Swiss-Prot: Q9BZQ4.1
Experimental Models: Cell Lines		
SH-SY5Y	ATCC	Cat#CRL-2266
HeLa	ATCC	Cat#CCL-2
INS-1	ATCC	Cat#CRL-2057
SK-Hep-1	ATCC	Cat#HTB-52
C6	ATCC	Cat#CCL-107
NCI-H295R	ATCC	Cat#CRL-2128
CAPAN-1	ATCC	Cat#HTB-79
JURKAT	ATCC	Cat#TIB-152
MeWo	ATCC	Cat#HTB-65
A375	ATCC	Cat#CRL-1619
SK-Mel-2	CRL-ITT, Pisa	N/A
SK-Mel-5	CRL-ITT, Pisa	N/A
SK-Mel-28	CRL-ITT, Pisa	N/A
M26C	CRL-ITT, Florence	N/A
M33x	CRL-ITT, Florence	N/A
U937	ATCC	Cat#CRL-1593
Experimental Models: Organisms/Strains		
Athymic nude mice (Foxn1 nu/nu)	Envigo	N/A

(*Continued on next page*)

Continued

REAGENT or RESOURCE	SOURCE	IDENTIFIER
Software and Algorithms		
VegaZZ	Drug Design Laboratory	http://www.vegazz.net
I-TASSER	Zhang Lab	http://zhanglab.ccmb.med.umich.edu/I-TASSER
Verify_3D	UCLA- DOE LAB	http://services.mbi.ucla.edu/Verify_3D/
Thermo ImageQuest	ThermoFisher	Cat#10137985
GraphPad Prism version 7.00 for Windows	GraphPad Software	https://www.graphpad.com/

CONTACT FOR REAGENT AND RESOURCE SHARING

Further information and requests for resources and reagents should be directed to and will be fulfilled by the Lead Contact Alberto Chiarugi (alberto.chiarugi@unifi.it)

EXPERIMENTAL MODEL AND SUBJECT DETAILS

Cell Culture

SH-SY5Y (gender female), HeLa (gender female), INS-1 (gender N/A), SK-Hep-1 (gender male), C6 (gender N/A), NCI-H295R (gender female), CAPAN-1 (gender male), JURKAT (gender male), MeWo (gender male) and A375 (gender female) cells were obtained from ATCC (Manassas, VA, USA). SK-Mel-2 (gender male), SK-Mel-5 (gender female) and SK-Mel-28 (gender male) melanoma cells were kindly provided by Laura Poliseno (CRL-ITT, Pisa, Italy). Patient-derived M26c (gender female) and M33x (gender female) melanoma cells were obtained from human melanoma samples after approved protocols by the Ethics Committee (Santini et al., 2014). Cells were grown in Dulbecco's modified Eagle's medium (DMEM) containing 25mM glucose and supplemented with 2mM glutamine, 1mM pyruvate, 10% fetal bovine serum and antibiotics. Mycoplasma was periodically tested by 4',6-diamidino-2-phenylindole (DAPI) inspection and PCR. Cultures were brought to 50-70% confluence and exposed to 100 μM of different compound. Compounds bearing the pyridinylmethyl-urea moiety were purchased by Specs Company (Bleiswijkseweg 55, 2712 PB Zoetermeer, The Netherlands) and dissolved in water with 4% of HCl 1N. FK866 and GMX1778 were dissolved in DMSO. NAD precursors were dissolved in culture media. Cell viability was assessed by 3-(4,5-dimethylthiazol-2-yl)-2,5-diphenyltetrazolium (MTT) assay and phase-contrast microscopy. Briefly, cells were detached with trypsin and EDTA, washed, resuspended in DMEM containing 3 μg/ml propidium iodide (PI) and incubated at 37°C for 10 min and then analysed by the flow cytometer Coulter EPICS XL (Beckman Coulter, Inc) equipped with the EXPO32 Flow Cytometry ADC software (Beckman Coulter, Inc).

In vivo Tumor Xenograft Model

All animal manipulations were performed according to the European Community guidelines for animal care (DL 116/92, application of the European Communities Council Directive 86/609/EEC). Adult (6 weeks) female athymic-nude mice (Foxn1 nu/nu) were used (Envigo, Udine, Italy). All mice were maintained in a pathogen-free animal facility for at least 1 week before each experiment. Mice were maintained in accordance with guidelines of the University of Florence for treatment and care of laboratory animals. Animals were implanted (day 0) on the right flank with $1x10^6$ SH-SY5Y (12 female mice per group) or $1,5x10^3$ M26C cells (14 female mice per group) in 100 μl of serum-free DMEM:matrigel 50:50. Tumors were measured daily with calipers, and volumes (V) calculated according to the formula $V=a2 \times b/2$, where *a* is the width in mm and *b* is the length in mm. Treatments (randomized and blinded) were initiated when the tumors were palpable. Statistical comparisons were made comparing control groups and treated groups using the Student's t test.

METHOD DETAILS

NAD, NADH and ATP Measurement

NAD contents were quantified by means of an enzymatic cycling procedure as described (Cipriani et al., 2005; Pittelli et al., 2010). Cells grown in a 48-well plate were killed with 1 N 50 μl of $HClO_4$ and then neutralized with an equal volume of 1 N KOH. After the addition of 100 μl of Bicine (100 mM), pH 8, 50 μl of the cell extract was mixed with an equal volume of the Bicine buffer containing 23 μl/ml of ethanol, 0.17 mg/ml of 3-(4,5-dimethylthiazol-2-yl)-2,5-diphenyltetrazolium, 0.57 mg/ml of phenazine ethosulfate, and 10 μg of alcohol dehydrogenase. The mixture was kept at room temperature for 10 min and then absorbance at 550 nm was measured (VICTOR^3, Perkin Elmer). Intracellular NADH content were measured by quantifying cell autofluorescence as previously reported (Pittelli et al., 2010). Briefly, autofluorescence was measured with a microscopic apparatus (Nikon 2000-TU) equipped with an UV filter and a CCD camera. Five microscopic fields were randomly acquired per each cell culture slide and processed for fluorescence quantitation (Metamorph/Metafluor software). Cellular ATP content was measured by means of an ATPlite kit (Perkin

Elmer, Milan). Briefly, cells grown in a 48-well plate were killed with 70 μl of lucifarese buffer and then 20 μl of D-luciferin were added. The production of light caused by the reaction of ATP with added luciferase and D-luciferin was evaluated after 5 min by means of a luminometer.

Evaluation of Mitochondrial Membrane Potential

Mitochondrial membrane potential (deltapsi(m)) was evaluated by means of flow cytometry. Cells seeded in 48 well plates were incubated with TMRE 2.5 nM in DMEM, exposed or not to Vacor 100 μM and analyzed. Cells exposed to FCCP 100 nM for 15 min were used as positive control. Briefly, cells were detached with trypsin and then diluted in DMEM. After gentle pipetting, 200 μl of the cell suspension were further diluted with PBS and analyzed by the flow cytometer Coulter EPICS XL (Beckman Coulter, Inc) equipped with the EXPO32 Flow Cytometry ADC software (Beckman Coulter, Inc). TMRE 2.5 nM was present in all the solutions used for cell preparation and measurement.

Cell Fractionation

Mitochondria and nuclei were isolated from cells ($1{,}5x10^6$) using a glass/glass homogenizer in 500 μl of extraction buffer (TRIS/MOPS 10mM, EGTA/TRIS 1mM, Sucrose 200mM, pH 7.4). Briefly, supernatants were first centrifuged for 10 min at 600 g to obtain nuclear fraction, and then were centrifuged for 15 min at 7000 g to obtain the mitochondrial pellet (Formentini et al., 2009). NAD formation was evaluated using the above-mentioned enzymatic cycling procedure.

Oxygen Consumption Analysis

Quantitation of oxygen consumption was conducted by means of the Oxygraph system (Hansatech Instruments, Norfolk, UK). Cells (250.000), exposed or not to Vacor 100 μM at different time, were gentle detached with trypsin and loaded in the chamber containing 350 μl of DMEM. Oxygen consumption was monitored for 8 min at 37°C.

Lactate Assay

Lactate levels were determined using a lactate assay kit according to the manufacturer's instructions (BioVision). Cells were seeded into 48-well plates, exposed or not to Vacor 100 μM at different time. Cells were homogenized in 100 μl of assay buffer and centrifuged to remove the insoluble materials. The soluble fraction was mixed to 50 μl Reaction Mix, the reaction was incubated for 30 min at room temperature, protected from light, and then fluorescence (Ex/Em = 535/590 nm) was measured. All data were normalized on cell protein content.

Radioactive Metabolic Assay

For the detection of CO_2 released from radioactive substrates, cells were incubated with 0.5μ Ci/ml [U-14C]-glucose for 15 min into 35 mm-dish. Each dish had a taped piece of Whatman paper facing the inside of the dish wetted with 100μl of phenyl-ethylamine-methanol (1:1:1) to trap the CO_2. Then 200μl of 4M H_2SO_4 was added to cells. Finally, Whatman paper was removed and transferred to scintillation vials for counting.

Preparation of Human Recombinant NAMPT and NMNATs

The coding region of human NAMPT was amplified from U937 monocyte cell line cDNA, and cloned into the pET15b vector at NdeI site. E. coli BL21 (DE3) cells transformed with the recombinant plasmid were grown at 37°C until an optical density at 600 nm of 0.6. After 20 min at 25°C, protein expression was induced using 0.8 mM IPTG. Cells were harvested after overnight induction at 25°C. Pellets were resuspended in one-fiftieth of the original culture volume with 50 mM HEPES/NaOH buffer, pH 7.5, 500 mM NaCl, 1 mM TCEP (lysis buffer), containing 10 mM imidazole, 1 mM PMSF and 0.05 ml/g cell pellet of Protease Inhibitor Cocktail. The suspension was sonicated three times for 1 min at 50 W, with 1 min intervals, and centrifuged at 20,000 x g for 30 min at 4°C. The supernatant deriving from 50 ml culture was loaded onto a HisTrap HP column equilibrated with 10 mM imidazole in lysis buffer. After washing with 40 mM imidazole in lysis buffer, elution was carried out by a linear increase of imidazole concentration up to 350 mM. Active fractions were passed through a PD-10 column equilibrated and eluted with 50 mM HEPES/NaOH buffer, pH 7.5, 300 mM NaCl, 20% glycerol. For the expression of the three human NMNAT isoenzymes, the constructs NMNAT1- pTrcHisA and NMNAT3-pTrcHisA were transformed into E.coli TOP10F cells, whereas NMNAT2-pET28c was transformed into E.coli BL21(DE3) cells.

Cultures were grown at 37°C in Luria-Bertani medium, supplemented with 100 μg/ml ampicillin (for NMNAT1 and NMNAT3) or with 50 μg/ml kanamycin (for NMNAT2). At an OD600nm of 0.6 proteins expression was induced with 1 mM IPTG. Cells expressing NMNAT1 and NMNAT3 were harvested after overnight induction at 37°C and cells expressing NMNAT2 were harvested after 5 h induction at 28°C.

Cell pellets were resuspended in one-twentieth of the original culture volume with the following lysis buffer: 50 mM sodium phosphate, pH 7.0, 300 mM NaCl, 5 mM CHAPSO (for NMNAT2), freshly supplemented with 1 mM PMSF, 1 mM TCEP, 0.05 ml/g cell pellet of Protease Inhibitor Cocktail. Suspensions were lysed by French Press (18 000 psi) and centrifuged at 20,000 x g for 20 min at 4°C. Supernatants deriving from 500 ml coltures were loaded onto HisTrap HP columns equilibrated with lysis buffers. After washing with 40 mM imidazole (for NMNAT1 and NMNAT3) and 20 mM imidazole (for NMNAT2) in the lysis buffers, elution was carried out by a

linear increase of imidazole concentration up to 350 mM. Active and homogeneous fractions were pooled and passed through PD-10 columns equilibrated and eluted with 50 mM HEPES/NaOH buffer, pH 7.5, 1 mM TCEP, 20% glycerol.

Preparation of VMN and VAD

A reaction mixture consisting of 0.4 mM Vacor, 1.4 mM PRPP, 1 mM ATP, 4.4 mU hNAMPT, 100 mU hNMNAT2 in 50 mM HEPES/KOH, pH 7.5, 20 mM $MgCl_2$, 0.5 mg/ml BSA, 1 mM TCEP (final volume 350 μl) was incubated overnight at 37°C. The reaction was stopped by adding 175 μl 1.2 N $HClO_4$, and after 10 min on ice the acidified mixture was centrifuged at 16,000 x g for 3 min. 500 μl of the supernatant were neutralized with 107 μl 1M K_2CO_3 and centrifuged as above. 100-μl aliquots of the supernatant were injected into a Kinetex C18 LC column (2.6 μm, 150 x 4.6 mm) equilibrated with 92% buffer A (100 mM ammonium acetate, pH 6.0), 8% buffer B (buffer A, containing 80% acetonitrile). Elution conditions were as follows: 5 min 8% buffer B, up to 50% buffer B in 10 min, hold to 50% buffer B for 5 min, down to 8% buffer B in 2 min, hold to 8% buffer B for 8 min. Flow rate was maintained at 0.75 ml/min, and temperature was fixed at 50°C. VAD, VMN and Vacor were eluted at 11, 14 and 17 min, respectively. In the assay conditions described above, Vacor was totally consumed, and 84% and 16% was found as VMN and VAD, respectively. Fractions corresponding to VMN and VAD were collected and lyophilized. Purity was verified by HPLC analysis after resuspension in 40 mM HCl. Quantitation was performed spectrophotometrically by using an extinction coefficient value at 340 nm of 17.8 M-1cm-1, which is the value we calculated for Vacor based on dry weight analysis.

Kinetic and Inhibition Studies on NAMPT and NMNATs

HPLC analyses - Unless otherwise stated, NAMPT and NMNAT assay mixtures consisted of 50 mM HEPES/KOH, pH 7.5, 20 mM $MgCl_2$, 0.5 mg/ml BSA, 1 mM TCEP and appropriate substrates and enzymes' amounts. After incubation at 37°C, reactions were stopped by acidification and neutralization, as described in Supplemental Information. For quantification of formed VMN, supernatants were injected into either a Kinetex HILIC LC column (2.6 μm 150 x 4.6 mm) or a Supelcosil LC-18-S column (5 μm, 250 x 4.6 mm). The former column was equilibrated and eluted with 100 mM ammonium acetate, pH 6.0, 4% acetonitrile, at 35°C and at a flow rate of 0.75 ml/min. The latter column, was equilibrated and eluted with 100 mM potassium phosphate buffer, pH 6.0, 8.0 mM tetrabutylammonium sulfate, 20% methanol, at 50°C and at a flow rate of 2.0 ml/min. The same column also allowed quantitation of VAD.

For NAD quantification, samples were injected into the Supelcosil LC-18-S column (5 μm; 250 x 4.6 mm) equilibrated with 100 mM potassium phosphate, pH 6.0, containing 8 mM tetrabutylammonium hydrogen sulfate (buffer A). NAD was eluted at flow-rate of 1 ml/min under the following gradient conditions: 4 min at 100% buffer A; 12.5 min up to 15% buffer B (buffer A plus 30% methanol); 23.5 min up to 90% buffer B; 7 min hold at 90% buffer B, followed by re-equilibration in buffer A. The column temperature was 8°C. (Mori et al., 2014).

VMN-synthesizing activity of NAMPT - For kinetic analysis, NAMPT assay mixtures containing 0.12 mU/ml hNAMPT, 1 mM PRPP, 1 mM ATP and VACOR concentrations ranging from 50 to 10 μM, were incubated at 37°C for 30 and 60 min. The formed VMN was quantified by HPLC analysis on the HILIC column.

VAD-synthesizing activity of NMNATs - To assess the VAD-synthesizing activity of the three human isoforms, assay mixtures containing 1 mM ATP, 50 μM VMN and 0.8 U/ml of each enzyme were incubated overnight at 37°C. The formed VAD was quantified by HPLC on the Supelcosil LC-18-S column.

For comparison with the NAD-synthesizing activity, analyses were performed under conditions of initial velocity. VAD synthesis was measured in mixtures containing 0.15 mM VMN, 1mM ATP and 0.4 U/m of each NMNAT isoform. NAD synthesis was measured in mixtures containing 0.15 mM NMN, 1 mM ATP and 1mU/ml of each isoenzyme. After 15 and 30 min incubation at 37°C, VAD and NAD were quantified by HPLC on the Supelcosil LC-18-S column, as described above.

For the kinetic analysis of the NMNAT2-catalyzed formation of VAD, assay mixtures containing 0.5 U/ml hNMNAT2, 1 mM ATP, and VMN concentrations ranging from 10 to 200 μM, were incubated at 37°C for 15 and 30 min. The formed VAD was quantified by HPLC analysis on the Supelcosil LC-18-S column. For comparison with the NMN adenylyltransferase activity, assay mixtures containing NMN in the place of VMN and 0.5 mU/ml hNMAT2 were incubated in parallel.

Effect of Vacor, VMN and VAD on NMNATs activity - The effect of Vacor on the three NMNAT isoforms was assayed in NMNAT mixtures containing 1 mM ATP, 20 μM NMN and 0.8 mU/ml of each NMNAT isoform, in the absence and in the presence of 0.1 and 0.4 mM VACOR. The effect of VAD was assayed in NMNAT mixtures containing 1 mM ATP, 20 μM NMN and 0.8 mU/ml of each NMNAT isoform, in the absence and in the presence of VAD concentrations ranging from 5 to 100 μM VAD. NAD formation was analyzed by HPLC after 10 and 20 min incubation at 37°C. The effect of VMN on the NMNAT2 activity was tested by varying NMN from 8 to 20 μM, with VMN ranging from 150 to 400 μM, at 1 mM ATP. The experimental initial rates were fitted to the equation:

$$v = \frac{V_{max}[S]}{K_M\left(1+\left(\frac{[I]}{K_i}\right)^n\right)+[S]\left(1+\left(\frac{[I]}{\alpha K_i}\right)^n\right)}$$

where Ki and αKi are the dissociation constants of the EIn and ESIn complexes, and n is the number of inhibitor molecules that bind the enzyme. Fitting was performed by means of an iterative non-linear least-squares procedure using Microsoft Excel software.

Effect of Vacor on NAMPT activity - The effect of Vacor on NAMPT activity was assayed by the coupled fluorometric cycling assay as described (Zamporlini et al., 2014). In particular, to determine the IC50 value for Nam, reaction mixtures consisting of 70 mM

HEPES pH 7.5, 10 mM $MgCl_2$, 0.4 mM PRPP, 2.5 mM ATP, 0.2 μM Nam, 0.002 mU/ml hNAMPT, and VACOR concentrations ranging from 0 to 2.5 μM, in a final volume of 60 μl were incubated at 37°C, in the presence of the ancillary enzymes PncC (1 mU) and NadD (30 mU). At 5 and 10 min incubation, reactions were stopped at 95°C for 1 min. 40 ul of the samples were transferred into the wells of a flat-bottomed 96-well black plate. The formed NAAD was converted to NAD in a buffer consisting of 50 mM HEPES/KOH, pH 7.5, 150 mM KCl, 1.4 mM ATP, 50 mM NH_4Cl, 11 mM $MgCl_2$, by adding 9 mU of ancillary enzyme NadE (final volume of 145 μl). After incubation for 30 min at 37°C, the formed NAD was cycled by adding 96 uL of a freshly prepared cycling reagent consisting of 100 mM sodium phosphate, pH 8.0, 2% ethanol, 32 μM Resazurin, 10 U/ml Alcohol Dehydrogenase (ADH), 0.1 mg/ml BSA, 10 uM Flavin Mononucleotide (FMN) and 0.1 mg/ml Diaphorase that was previously purified through a PD MiniTrap G-25 column equilibrated and eluted with 10 mM sodium phosphate buffer, pH 8.0. The resorufin fluorescence was measured continuously using a Synergy HT microplate reader (Bio-Tek, Winooski VT, USA) set at excitation and emission wavelengths of 544 and 590 nm, respectively. The rates of fluorescence increase in individual wells were recorded and plotted against the incubation time. The slope of the regression line was used to calculate the NAMPT activity by referring to a NAAD standard curve (Zamporlini et al., 2014).

Suitable control mixtures were processed in parallel to rule out the effect of VACOR on the ancillary system. The same assay was used to determine the Ki with respect to PRPP. In the reaction mixtures, Nam was fixed at 1 μM and PRPP varied from 0.25 to 5 μM. Vacor concentrations ranged from 10 to 50 μM, and reactions were stopped after 5 and 10 min incubation. Ki value was calculated from the replot of the slopes of the reciprocal plot against [I] (Segel, 1993).

Effect of VAD on Dehydrogenases Activity

GA3PDH activity was assayed in 50 mM sodium phosphate buffer, pH 8.0, 13 mM 3-phosphate glyceraldehyde, 30 μM NAD and 0.14 mU/ml enzyme from chicken muscle in the absence and in the presence of different VAD concentrations. IMPDH activity was assayed in 100 mM TRIS-HCl, pH 8.0, 100 mM KCl, 2 mM EDTA, 1 mM DTT, 0.1 mM IMP, 30 μM NAD and 0.12 mU/ml recombinant human IMPDH, type II, in the absence and in the presence of different VAD concentrations. After 5 and 10 min incubation at 37°C, reactions were stopped by heating at 100°C for 1 min. Formed NADH was quantitated by HPLC analysis on a Supelcosil LC-18-T column (5 μm, 250 x 4.6 mm) equilibrated with 100 mM potassium phosphate, pH 6.0 (buffer A) .The elutions conditions were as follows: 9 min at 100 % buffer A, 6 min at up to 12% buffer B (buffer A plus 20% methanol), 2.5 min at up to 45% buffer B, 2.5 min at up to 100% buffer B, and hold at 100% buffer B for 5.5 min. Finally, the gradient returned to 100% buffer A in 5 min. The column was flushed with buffer A for 4.5 min prior to next run. The flow rate was 1.3 ml/min and the column was thermostatted at 18°C (Balducci et al., 1995).

To characterize the GA3PDH-VAD interaction, the enzyme activity was assayed in the presence of concentrations of NAD ranging from 10 to 40 μM, and VAD ranging from 50 to 100 μM, at fixed 13 mM 3-phosphate glyceraldehyde. Kinetic parameters and inhibitor constants were determined by using the Lineweaver-Burk plot and the slope and intercept replots as described in (Segel, 1993).

Determination of Nucleotides and Vacor Metabolites in Cell Lysates

Nucleotides were extracted from SH-SY5Y, M26C or HeLa cell by resuspending cell pellets in 0.4M $HClO_4$. After 5 min on ice, samples were centrifuged at 16,000 x g for 3 min. Pellets were resuspended in formic acid for proteins determination by means of the Bradford assay, and supernatants were neutralized with 1M K_2CO_3 and centrifuged as above. For VACOR, VMN and VAD determination, neutralized supernatants corresponding to about 0.4 mg proteins for SH-SY5Y and M26C cells and 1.4 mg proteins for HeLa cells were injected into a Supelcosil LC-18-S colum equilibrated with 33% buffer A (100 mM potassium phosphate buffer, pH 6.0, 8.0 mM tetrabutylammonium sulfate) and 67 % buffer B (buffer A containing 30% methanol). Elution conditions were as follows: 16 min 67% buffer B, up to 100% buffer B in 1 min, hold to 100% buffer B for 18 min, down to 67% buffer B in 5 min, hold to 67% buffer B for 5 min. Flow rate was maintained at 2.0 ml/min, and temperature was fixed at 50°C. For NAD determination, neutralized samples corresponding to about 0.2 mg proteins were injected into the same column eluted as described above (Mori et al., 2014). NMN was measured upon derivatization with acetophenone and spectrofluorometric HPLC analysis (Mori et al., 2014). Derivatization was performed by mixing up to 50 μl of neutralized samples corresponding to about 0.1 mg proteins with 100 μl KOH 1N and 50 μl acetophenone. After 15 min incubation at 4°C, 100 μl of formic acid was added and the samples were heated for 5 min at 100°C. Aliquots of 195-μl were injected onto a Tracer Extrasil ODS2 column (5 μm, 250 x 4.0 mm) connected to a Perkin Elmer LS-45 spectrofluorometer set at excitation and emission wavelengths of 380 and 440 nm, respectively. Column equilibration was performed using 100 mM potassium phosphate buffer, pH 2.1, containing 10% acetonitrile (buffer A). The elution gradient was: 6 min at 100% buffer A, 5 min up to 100% buffer B (buffer A plus 40% acetonitrile), 6 min hold at 100% buffer B, followed by re-equilibration in buffer A. The column temperature and the flow rate were 25°C and 1.5 ml/min, respectively.

Measurements were performed by using a duplicate sample analyzed in parallel and containing known amounts of NMN spike.

Molecular Modeling

NAMPT file 4L4L.pdb (Oh et al., 2014) was retrieved from pdb database [www.rcsb.org] directly by MolProbity server [http://molprobity.biochem.duke.edu] where the file was checked and hydrogen atoms added. The resulting new pdb file was passed for further elaborations to the software VegaZZ (ver. 3.1.0) (Pedretti et al., 2004). Indeed, VegaZZ package, was employed as a front-end to prepare, launch and analyze AutoDock Vina (Trott and Olson, 2010) calculations: 3D coordinates were normalized, water molecules and other ligands were removed from the pdb file; all ligands were built by using the sketcher, their coordinates were then 3D converted and minimized. Scripts incluted in VegaZZ such as Receptor.c and Ligand.c were then used for protein and ligands

preparation. The region of interest used by AutoDock Vina for docking was centered at about 10Å around the cocrystallized ligand on 4L4L.pdb. Thus, the following parameters were used: center_x = 13.63, center_y = 8.30, center_z = 4.44; size_x = 25, size_y = 20, size_z = 30; exhaustiveness = 64; num_modes = 10, other parameters were as default.

NMNAT2 3D structures were modeled by comparative modeling using I-TASSER server (Roy et al., 2010; Yang et al., 2015) using the sequence of the human NMNAT2 (UniProtcode Q9BZQ4.1). Five 3D models of were generated and passed to another online tool Verify_3D (Luthy et al., 1992); for the assessment of the model's quality. The coordinates of the selected model4 were normalized by VegaZZ and submitted to the docking simulations with AutoDockVina: the whole protein was used for the blind docking using a large box of 60Å for each side centered at the centre of the protein, other AutoDockVina methods and parameters were as before. Finally, binding poses, with the lowest docked energy belong to the top 10 ranked modes of each ligands, in the corresponding proteins were selected and analyzed by visual inspection. LigPlot+ (ver. 1.4.5) (Laskowski and Swindells, 2011) and Chimera (ver. 1.10) (Pettersen et al., 2004) were further employed for protein-ligand complex visualization, analysis and rendering.

RNA Isolation and qPCR

Total RNA was isolated using Trizol Reagent (Life Technologies). One μg of RNA was retrotranscribed using iScript (Bio-Rad, Milan, Italy). Real-Time PCR was performed using Rotor-Gene 3000 (Qiagen, Milan, Italy) and the Rotor-Gene TM SYBR® Green PCR Kit (Qiagen, Milan, Italy), the reactions were run at 95°C for 30 seconds, 95°C for 5 seconds and 60°C for 15 seconds for 45 cycles. The following primers were used: human 18S 5'-CGGCTACCACATCCAAGGAA-3' (sense), 5'-GCTGGAATTACCGCGGCT-3' (antisense); human NMNAT1 5'-TCCCATCACCAACATGCACC -3' (sense), 5'-TGATGACCCGGTGATAGGCAG -3' (antisense); human NMNAT2 5'- GATTGGATCAGGGTGGACC -3' (sense), 5'- TCCGATCACAGGTGTCATGG -3' (antisense); rat 18S 5'-AAAACCAACC CGGTGAGCTCCCTC -3' (sense), 5'-CTCAGGCTCCCTCTCCGGAATCG -3' (antisense); rat NMNAT1 5'-CAGCCCACCACCGAAT CATC -3' (sense), 5'- TTTCCAGCACAGGTGAGCTTT -3' (antisense); rat NMNAT2 5'- GCAGGCTGGCCCTGCAGCAT-3' (sense), 5'- GAGGCAGGAGAGAAACCGGGG -3' (antisense) (IDT Tema Ricerca, Bologna, Italy).

MS Imaging

Tumor specimens were frozen under nitrogen vapors and stored at -80°. The tissue was then cryosectioned (CM 1850-1, Leica, Germany) at 10 μm slice thickness and posed on histology glasses (Superfrost Plus, Menzel, Germany). ImagePrep (Bruker Daltonik GmbH, Germany) device was used for uniform spray coating of the glasses, using customized methods that assured the deposition of approximately 10 mg of matrices for every slide. MS-Imaging analyses were performed on a MALDI-LTQ-Orbitrap XL equipped with a nitrogen laser at 60 Hz. The MALDI matrix used for Vacor detection was HCCA (α-cyano-hydroxycynnamic acid) posed at 10 g/L in a solution formed by 50:50:0.2 H2O:AcCN:TFA with addition of aniline in equimolar quantity with HCCA. Matrix for ATP and AMP detection was 9-aminoacridine posed at 1 g/L in 50:50 H2O:AcCN.

ESI- HRMS Electrospray High Resolution Mass Spectrometry

The residue of the HPLC fractions was re-suspended in 100 uL of a mixture of water and acetonitrile (1:1, v/v) containing 0.1% formic acid. The solution was analysed by infusion (at 3 uL/min flow rate) in the ESI interface of a LTQ Orbitrap, a hybrid linear ion trap orbitrap high resolution mass spectrometer (Thermo Fisher Scientific, Bremen, Germany). Spectra were recorded in positive ion mode, in scan mode in the 50-1000 m/z range, operating at 100000 resolution (at m/z 400). The ESI parameters were as follows: spray voltage 5 kV, capillary voltage 48 V, capillary temperature 275°C, tube lens voltage 160 V; nitrogen were used as nebuliser and auxiliary gas, at 8 and 3 values (arbitrary units), respectively. Data were acquired and analysed using the Xcalibur software (ver. 3.0). As for NMN or VMN detection in culture media, sample of media from Hela cells exposed to NAD or VAD 1mM/1h were extracted with methanol and centrifuged at 12,500 × g for 30 min at 4°C. Supernatants were lyophilized, resuspended in water and acetonitrile (1:1, v/v) containing 0.1% formic acid and analysed as descripted above.

QUANTIFICATION AND STATISTICAL ANALYSIS

All data represent the mean and SEM of at least 2 independent experiments. All differences were statistically evaluated comparing treated and untreated conditions using ANOVA plus Tukey's post hoc test. Levels of significance were $p<0.05$ (*), $p<0.01$ (**). Statistical analyses were carried out using GraphPad Prism (version 7). NADH fluorescence quantitation levels were acquired and processed using Metamorph/Metafluor software. High Resolution Mass Spectrometry data were acquired and analysed using the Xcalibur software (ver. 3.0).

DATA AND SOFTWARE AVAILABILITY

The accession number for the sequence of the human NMNAT2 reported in this paper is UniProtKB/Swiss-Prot: Q9BZQ4.1.